DESIGN OF VIBRATION ISOLATION SYSTEMS THAT INCORPORATE AXIAL TO ROTARY MOTION CONVERSION MECHANISMS

by

Adil Han Orta

B.S., Mechanical Engineering, Boğaziçi University, 2015

Submitted to the Institute for Graduate Studies in
Science and Engineering in partial fulfillment of
the requirements for the degree of
Master of Science

Graduate Program in Mechanical Engineering

Boğaziçi University

2018

ACKNOWLEDGEMENTS

First of all, I would like to thank Assoc. Prof. Çetin Yılmaz for supervising this thesis with his innovative ideas, endless support, patience and guidance throughout my entire graduate study. I would like to thank him for being such a great mentor.

I also acknowledge Assoc. Prof. Serdar Soyöz and Assist. Prof. Polat Şendur, for their precious times to read this thesis and giving critical comments about it.

I would like to acknowledge my friends Ayşen and Eren for their encouragement and support.

I would like to thank to Borusan Arge and my unit manager İskender Kayabaşı for their support.

Finally, I would like to thank to my family for their encouragement and emotional support. They always motivated me.

This work was supported by Bogazici University Research Fund with Grant Number 16A06P4.

ABSTRACT

DESIGN OF VIBRATION ISOLATION SYSTEMS THAT INCORPORATE AXIAL TO ROTARY MOTION CONVERSION MECHANISMS

In this thesis, compliant axial to rotary motion conversion mechanisms are examined to generate isolation band gaps. To achieve low frequency phononic band gaps, LADD mechanism is examined, and its the effective inertia is aimed to be amplified. Moreover, to increase the isolation band gap of this structure, helical wire theory is investigated, and both analytical and finite element models of the mechanism are created and validated with experiments. Then, by applying prestress and optimizing the cross section area of the helical wires, the phononic band gap is maximized at low frequencies. A quite wide band gap with ω_1/ω_2=0.215 is obtained with the use of idealized roller boundary conditions. However, this type of boundary condition is compliantly realized via wires, the frequency ratio (ω_1/ω_2) increased to 0.5 and the band gap became narrower. Therefore, a novel axial to rotary motion conversion mechanism is proposed. In the proposed unit cell, a stop band is governed by two different types of modes. The lower and the upper natural frequencies of stop band is limited by the coupled axial-torsional and bending modes, respectively. For stop band maximization, cross and spiral flexures are used due to their high bending stiffness and low axial stiffness. Besides, helical wires with large pitch angle are utilized to create large rotational motion from axial translations. Thus, the effective inertia of the mechanism is amplified. By using analytical and finite element models, band structure and the dynamic response attributes of the structure are examined, and parametric studies are conducted. 3D printing and laser cutting is used during prototyping. Finally, comparison of the analytical, computational and experimental frequency response results is held for validation. In conclusion, a very wide phononic band is obtained with ω_1/ω_2=0.221.

ÖZET

EKSENEL HAREKETİ DÖNME HAREKETİNE ÇEVİREN ATALET ARTIRIM MEKANİZMASI TASARIMI

Bu tezde, titreşim yalıtım bant aralıkları oluşturmak amacıyla esnek bağlantılı eksenel hareketi dönme hareketine çeviren mekanizmalar incelenmiştir. Düşük frekanslarda fonon bant aralıkları elde edebilmek için LADD mekanizması incelenmiş ve efektif ataleti arttırılmaya çalışılmıştır. Ayrıca, yalıtım bant aralıklarının genişletilmesi amacıyla helisel teller araştırılmış, analitik ve sonlu eleman modelleri yaratılmıştır. Kurulan modeller deneylerle doğrulanmıştır. Sonra yapıya öngerilme uygulanarak ve helisel tellerin kesit alanları eniyilenerek yapının fonon bant aralığı düşük frekanslarda maksimize edilmiştir. Oldukça geniş bir bant aralığı ω_1/ω_2=0.215 frekans oranı ve idealize edilmiş basit mesnet sınır koşullarıyla elde edilmiştir. Ancak bu tip bir sınır koşulu esnek bağlantılı teller aracılığıyla realize edilmeye çalışıldığında frekans oranı (ω_1/ω_2) 0.5'e çıkmış ve bant aralığı daralmıştır. Bu sebeple eksenel hareketi dönme hareketine çeviren özgün bir yapı önerilmiştir. Önerilen birim hücrede yalıtım bant aralığının iki farklı mod şekline bağlı olduğu görülmüştür. Yalıtım bandının alt ve üst frekans limitleri sırasıyla eksenel-dönme ve eğilme moduna bağlıdır. Yalıtım bant aralığının maksimize edilmesi amacıyla çapraz ve spiral esnek bağlantı mekanizmaları yüksek eğilme ve düşük eksenel rijitliğe sahip olduğu için kullanılmıştır. Ek olarak, yüksek helis açılı teller eksenel hareketten dönme hareketi sağlamak için kullanılmıştır. Böylece sistemin efektif ataleti arttırılmıştır. Parametrik çalışmalar sayesinde düşük frekaslarda geniş bant aralıkları elde edilmiştir. Birim hücre ve periyodik yapıların prototipleri 3 boyutlu yazıcı ve lazer kesim metotlarıyla üretilmiştir. Son olarak, analitik, sonlu eleman ve deney sonuçları doğrulama amacıyla karşılaştırılmıştır. Sonuçta düşük frekansta çok geniş fonon bant aralığı (ω_1/ω_2=0.221) elde edilmiştir.

TABLE OF CONTENTS

LIST OF FIGURES

LIST OF TABLES

LIST OF SYMBOLS

A	Area of helical wire
d_{bolt}	Bolt diameter
E	Elastic modulus
g	Gravitational acceleration
G	Shear modulus
G_i	Flexural couples of the i^{th} direction in helical wire model
h	Cross flexure ring height
H	Torsional couple
I	Mass moment of inertia of the proposed mechanism
I_i	Area moment of inertia of the i^{th} direction in helical wire model
I_p	Polar moment of inertia of the helical wire
k	Spring stiffness
k_{eff}	Effective stiffness
k_{eq}	Equivalent stiffness
K_g	Beam gravity stiffness matrix
K_l	Beam stiffness matrix
k_s	Spiral spring stiffness
$k_{t_{cross}}$	Torsional stiffness of cross flexure
k_w	Wire stiffness
L	Lagrangian
L_{beam}	Beam Length
L_{bolt}	Bolt Length
m	Mass
m_a	Point mass attached to the lumped parameter model
m_b	Bending moment
m_t	Twisting moment
m_{eff}	Effective mass
M_l	Local mass matrix

n	Number of active coils
N_i	Shear Force of the i^{th} direction
p	Pitch
P	Applied spring tension
r	Coil radius after deformation
R	Tension at wires
r_0	Coil radius before deformation
s	Arc coordinate of the helical wire
t	Plate thickness
T	Kinetic energy
t_{beam}	Beam thickness
T_s	Applied spring torque
TR	Transmissibility
TR_∞	Transmissibility when natural frequency go infinity
u_v	Vertical displacement
u_h	Horizontal displacement
v	Poisson ratio
V	Potential energy
w_{beam}	Beam width
x	Lumped parameter model output
x_i	Axial translation of proposed mechanism
X	External couple along x axis
y	Lumped parameter model input
Y	External couple along y axis
Z	External couple along z axis
α	Helix angle after deformation
α_0	Helix angle before deformation
β	Angular displacement of disk
β_i	Angular displacement of the proposed mechanism at the i^{th} disk
δ	Deflection

$\Delta\theta$	Twist
ΔL	Elongation
ϵ_x	Strain
γ	Wave number
ϕ	Rotation matrix
Φ	Transformation matrix
θ	Lumped parameter model angular coordinate
ω_p	Resonance frequency
ω_z	Antiresonance frequency
κ	Curvature of helix in x direction
λ	Curvature of helix in y direction
τ	Twist of helix

LIST OF ACRONYMS/ABBREVIATIONS

1D	One Dimensional
2D	Two Dimensional
3D	Three Dimensional
CAD	Computer Aided Design
DOF	Degree of Freedom
FEA	Finite Element Analysis
FEM	Finite Element Method
LADD	Linear-to-Angular-Displacement-Device
SDOF	Single Degree of Freedom

1. INTRODUCTION

Motion conversion mechanisms are one of the fundamental topics of mechanical engineering [1–3]. Different mechanisms are used widely in the industry from robotics to automotive. These mechanisms can be examined with respect to their links as rigid or flexible.

In traditional mechanisms, links and hinges are rigid, and friction and backlash may be observed [4]. Flexible or compliant mechanisms create an alternative to rigidly connected mechanisms, and they consist of the connection of parts that can be bent [5]. Thus, hinges, which lack friction and backlash problem in rotational motion (at small angles) have been obtained.

1.1. Axial to Rotary Motion Conversion Mechanism with respect to Joints

1.1.1. Rigid Mechanisms

Slider-crank mechanism, rack and pinion and screw-nut mechanism are the most commonly used rigidly connected mechanisms that convert axial motion into rotary motion and vice versa. Slider-crank mechanisms are generally used to obtain rotary motion from axial motion (Figure 1.1(a)). However, this system is not linear. In the literature, many studies can be found about the optimization of link lengths, transmission angle, and angular speed to obtain maximum rotation for planar slider-crank mechanisms [6, 7]. In rack and pinion mechanism, linear motion of rack creates rotary motion at the gear (Figure 1.1(b)). However, in these mechanisms friction can create a problem [8]. Rack and pinion mechanism is used in a new device called "Inerter" [9,10]. This device can be utilized in vehicle suspension systems to obtain rotary motion from linear motion. Besides, a flywheel can be attached to the gear to increase the inertia of the system. However, the problems in gear mechanisms are valid for this system, too. Friction, backlash and elastic effects create non-linear deviations from the analytical results [11]. In screw and nut mechanism (Figure 1.1(c)), the rotation of nut creates

a linear motion for the screw. This system is linear, but the contact of screw and nut creates friction problem [12, 13].

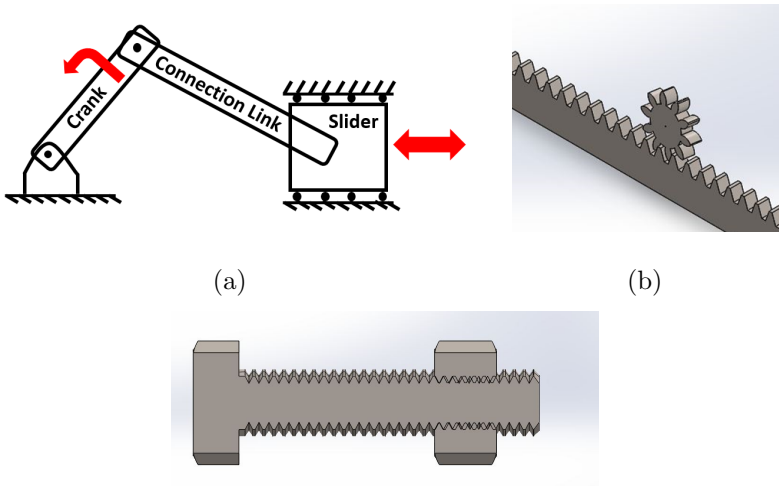

(a) (b)

(c)

Figure 1.1. Different Types of Rigid Link Mechanisms, (a) Slider-Crank, (b) Rack and Pinion, (c) Screw-Nut.

1.1.2. Flexible Mechanisms

Flexure mechanisms that convert axial motion to rotational one generally have helical structures. Twisted and stretched wires [14], LADD (Linear-to-Angular-Displacement-Device) mechanisms [15], helical nanotubes [16] and helical springs [17] are the main examples of helical flexure mechanisms. Twisted and stretched wires are generally used to measure displacement values of mechanical systems. This procedure depends on the difference between the length of stretched wire (without twist) and twisted wire. This difference is compared to the amount of rotation and it gives the displacement of the system [14, 15, 18]. LADD mechanism is another way to convert rotary motion to axial one and it is commonly used in robotic, manipulator and prosthetic devices. It consists of multiple cells and each cell has 2 rings (see Figure 1.2(a)). These rings are connected to other cells. Rotation of one ring creates rotation for all rings, and it creates a path for motion [19, 20]. Motions of helical micro or nanotubes are similar to other helical flexure mechanisms [16, 17, 21–23]. The connection of right and left-handed helical structures can create rotational motion at the connection point when it is pulled from both sides (see Figure 1.2(b)) [24–27]. Finally, helical springs can

be used to obtain axial to rotary motion conversion mechanism. These systems are generally utilized to measure strain under tension and/or compression. They are also used for the calibration of the strain measurement devices. For this reason, there are a lot of studies on this topic in the literature. Arbitrary wire cross-sectional shapes [28, 29], optimization of spring weight [30] and applied force change [31, 32] have been investigated in the literature. Besides, helical springs can be used for strain measurement of superconducting wires, as well [33–35].

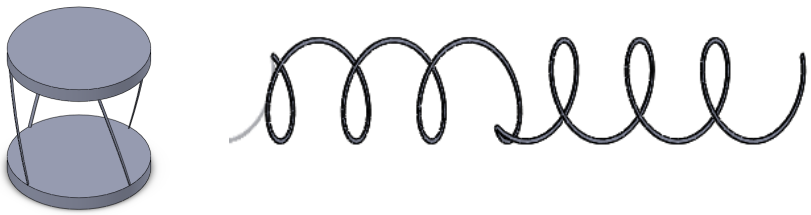

(a) (b)

Figure 1.2. Different Types of Flexible Link Mechanisms, (a) Unit LADD Cell, (b) Combination of Left Handed and Right Handed Helical Springs.

1.2. Band Gap Generation Methods

Periodic structures are studied considering their wave propagation characteristics in the literature [36, 37]. Infinite periodic structures can prevent wave propagation in certain frequency ranges. Frequency ranges in which acoustic or elastic waves do not propagate are called phononic band gaps [38, 39]. In contrast to infinite periodic structures, some amount of wave or vibration transmission is observed in finite periodic structures even if excited within band gaps. This wave or vibration transmission can be found by the examination of frequency response function diagrams. Finite periodic phononic band gap structures can be used for filtering mechanical vibrations, and utilized in noise and vibration isolation systems, and acoustic or elastic wave guides. For this reason, the maximization of isolation bandwidths and isolation effectiveness within the bandwidth are very important for practical applications. There are two main methods used to create phononic band gaps in a periodic medium. These are Bragg scattering and local resonances.

Bragg scattering is commonly used to obtain phononic band gaps for acoustic and elastic waves [37, 40, 41]. In this method, wave speed and lattice parameter determine the lowest phononic band gap. Consequently, materials that have high density/low elastic modulus or large sized periodic structures have to be chosen to obtain band gaps at low frequencies. However, these requirements create practical challenges for low frequency applications. A mass-spring array system, shown in Figure 1.3(a), is a 1D periodic structure of Bragg scattering which is used to achieve a band gap.

Band structure of the system can be obtained by analyzing the unit cell which is given in Figure 1.3(b), and the equation of motion are given in Equation 1.1 and Equation 1.2.

$$m_1\ddot{x}_1^{(i)} + 2kx_1^{(i)} - kx_2^{(i-1)} - kx_2^{(i)} = 0 \tag{1.1}$$

$$m_2\ddot{x}_2^{(i)} + 2kx_2^{(i)} - kx_1^{(i)} - kx_1^{(i+1)} = 0 \tag{1.2}$$

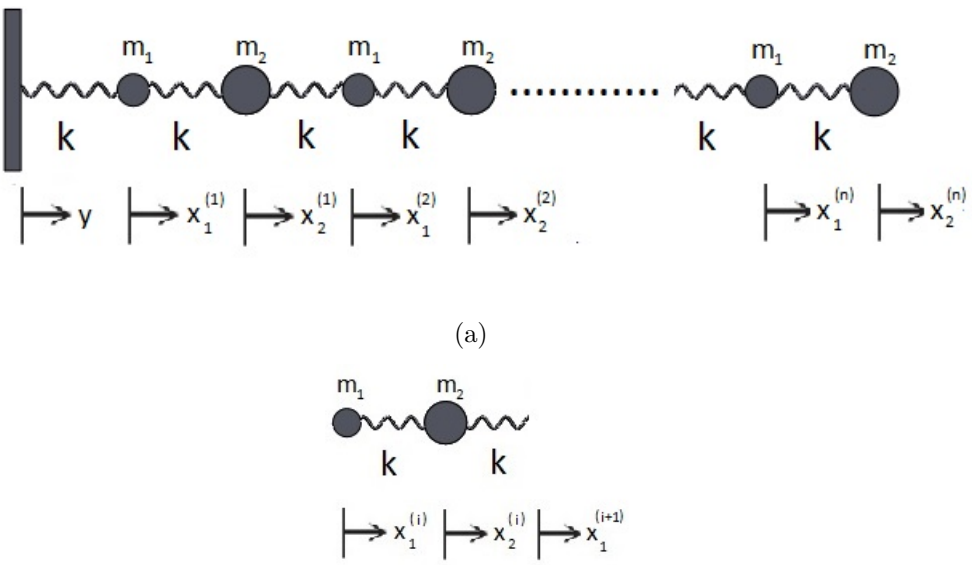

Figure 1.3. (a) Mass-Spring Array to Create Band Gap with Bragg Scattering, (b) Unit Cell of Bragg Scattering.

Bloch's theorem can be used to estimate the band structure of the system [36].

$$x_j^{(n+m)} = x_j^{(n)} e^{i\gamma T_m} \tag{1.3}$$

where T is the transformation matrix which is gives the orientation of $(n+m)^{th}$ unit with respect to $(n)^{th}$ one, and γ is the wave vector, which can be written as $\gamma = 2\pi ad$, where d is the length of the unit and a is the wave number, defined as $a = 1/\lambda$. The physically minimum possible wavelength is $2d$, and energy of any higher frequency wave cannot transmitted through the lattice. For this reason, a_{max} is $1/2d$, and wave vector limiting value is $\gamma_{max} = \pi$. Since the system is one dimensional, T =1. Thus, Equation 1.1 and Equation 1.2 can be rewritten as

$$m_1 \ddot{x}_1^{(i)} + 2kx_1^{(i)} - kx_2^{(i)}(1 + e^{-i\gamma}) = 0 \tag{1.4}$$

$$m_2 \ddot{x}_2^{(i)} + 2kx_2^{(i)} - kx_1^{(i)}(1 + e^{i\gamma}) = 0 \tag{1.5}$$

When Equation 1.4 and Equation 1.5 are solved for γ between 0 and π for different mass ratios, band structure can be obtained as in Figure 1.4. Here, k is taken as 2 N/m, and $m_1 + m_2$ =0.2 kg. Band structure plot shows that band gap is wider for the lower mass ratio $\mu = m_1/(m_1 + m_2)$.

Local resonance (resonance scattering) is another method to create phononic band gap in a structure. It can create band gaps at much lower frequencies than Bragg scattering [42–44]. Rubber coated dense metals in a epoxy matrix can be used to create local resonances at low frequencies [42]. In this method, the gap size and the gap center frequencies are dependent on volume filling fraction, and independent of the geometric arrangement of the local resonators [45]. However, large volume fractions require larger mass because the density of the coated inclusions are higher than the

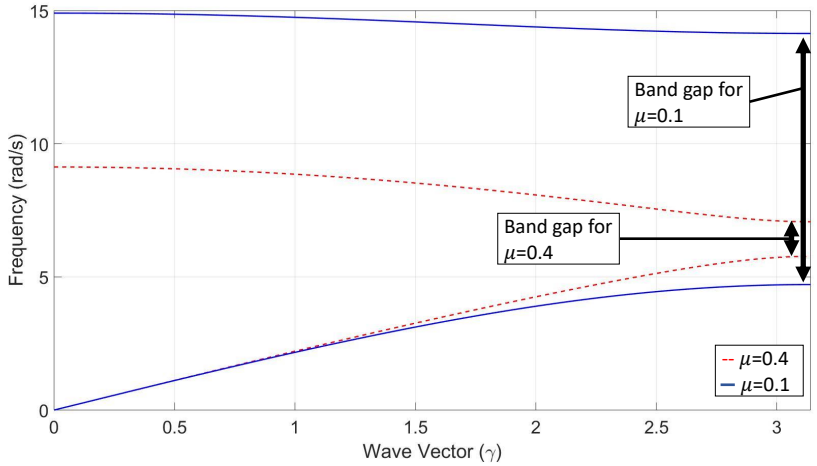

Figure 1.4. Band Structure Plot of Unit Cell of Bragg Scattering. Here, $\mu = m_1/(m_1 + m_2)$.

matrix. Realizing heavy resonators in small size structures is a hard design problem. Sketch of a local resonators attached to each unit cell is given in Figure 1.5(a).

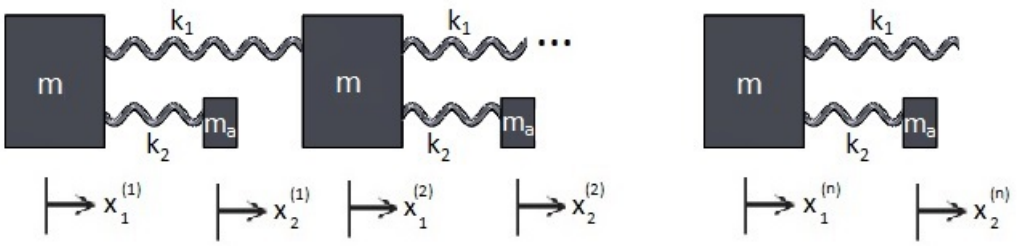

(a) (b)

Figure 1.5. (a) Resonators Attached to Each Unit Cell to Create Band Gap with Resonance Scattering, (b) Unit Cell of Resonance Scattering.

Unit cell (see Figure 1.5(b)) of the system is analysed and equation of motions are found as

$$m\ddot{x}_1^{(n)} + k_1\left(2x_1^{(n)} - x_1^{(n-1)} - x_1^{(n+1)}\right) + k_2\left(x_1^{(n)} - x_2^{(n)}\right) = 0 \tag{1.6}$$

$$m_a\ddot{x}_2^{(n)} + k_2\left(x_2^{(n)} - x_1^{(n)}\right) = 0 \tag{1.7}$$

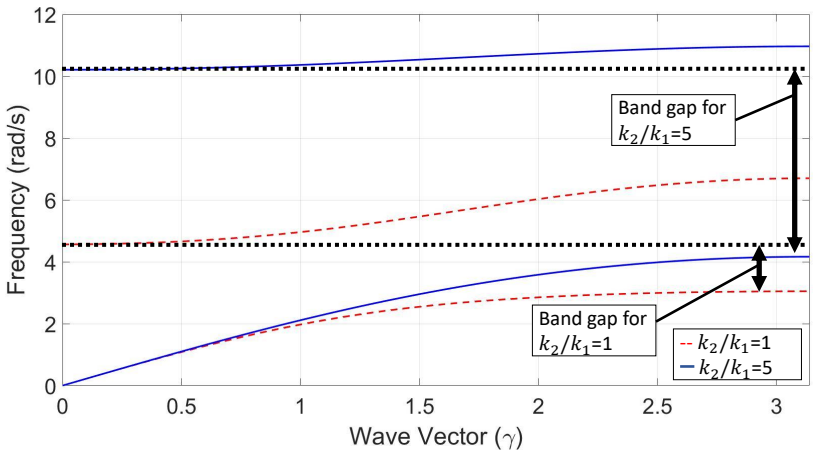

Figure 1.6. Band Structure Plot of Unit Cell of Resonance Scattering.

Using Bloch's theorem, equations of motions can be rewritten as

$$m\ddot{x}_1^{(n)} + k_1\left(2 - e^{-i\gamma} - e^{i\gamma}\right) + k_2\left(x_1^{(n)} - x_2^{(n)}\right) = 0 \tag{1.8}$$

$$m_a\ddot{x}_2^{(n)} + k_2\left(x_2^{(n)} - x_1^{(n)}\right) = 0 \tag{1.9}$$

Equation 1.8 and Equation 1.9 are solved for γ between 0 and π with different stiffness ratios. Band structure can be seen in Figure 1.6. Here, k_1 taken as 1 N/m, $m+m_a$ =0.2 kg, and $\mu = m_a/(m + m_a)$ =0.4. With these parameters, the total mass and end to end stiffness of the unit cell is the same when compared to the Bragg unit cell. Band structure plot show that wider band gaps can be obtained by increasing the stiffness ratio k_2/k_1. However, by decreasing the stiffness ratio k_2/k_1, band gap can be obtained at a lower frequency.

Recently, an alternative method based on inertial amplification has been found [38, 39]. Embedded inertial amplification mechanisms are investigated in 2D and 3D lumped parameter structures [38, 39, 46]. 1D, 2D and 3D distributed parameter structures [47–50] are examined to obtain wide phononic band gaps. Moreover, it is possible to obtain low frequency band gaps using inertial amplification mechanisms with host structures [51–54]. The studies show that the disadvantages of Bragg scattering and

local resonators can be eliminated with the inertial amplification method. By only increasing the amplification ratio (without changing the mass or the stiffness of the system), frequency band gap can be decreased. Sketch of a 1D inertial amplification is given in Figure 1.7(a).

When the unit cell of the inertial amplification mechanism is examined, shown in Figure 1.7(b), if connected links of m_a are rigid, then there will be no additional degree of freedom in the system (u_v and u_h can be written in terms of x_1 and x_2). Increasing the effective inertia is possible due to the amplified inertial forces generated by the mass m_a. Additionally, effective inertia of the system can be much larger than the total mass for small θ value. This will be shown by analysing the equation of motion of the system.

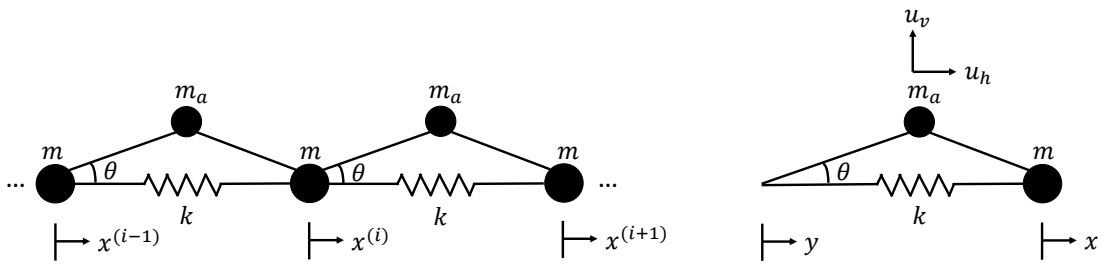

(a) (b)

Figure 1.7. (a) A 1D Array of Inertial Amplification Mechanism, (b) Lumped Parameter Model of the Inertial Amplification Mechanism.

For small θ values, the displacement at the end of the spring and the point mass is amplified. Equation 1.10 and Equation 1.11 show the relationship between displacement of the ends and point mass.

$$u_v = \frac{y + x}{2} \tag{1.10}$$

$$u_h = \frac{y - x}{2} \cot\theta \tag{1.11}$$

where u_v and u_h are the vertical and horizontal displacements of the attached point mass, respectively. The potential energy (V) and the kinetic energy (T) of the lumped parameter model (see Figure 1.7(b)) can be calculated with Lagrange's method [55] given in Equation 1.12.

$$\frac{d}{dt}\left(\frac{\partial L}{\partial \dot{x}}\right) - \frac{\partial L}{\partial x} = 0 \tag{1.12}$$

where $L = T - V$. The potential and kinetic energy can be written as in Equation 1.13 and Equation 1.14, respectively.

$$V = \frac{1}{2}k(y-x)^2 \tag{1.13}$$

$$T = \frac{1}{2}m_a\left(\left(\frac{\dot{y}+\dot{x}}{2}\right)^2 + \left(\frac{\dot{y}-\dot{x}}{2}\cot\theta\right)^2\right) + \frac{1}{2}m\dot{x}^2 \tag{1.14}$$

Finally, equation of motion of the lumped parameter model can be found as

$$\left(m + m_a(\cot^2\theta + 1)/4\right)\ddot{x} + kx = \left(m_a(\cot^2\theta - 1)/4\right)\ddot{y} + ky \tag{1.15}$$

The effective mass and the equivalent stiffness can be obtained by Equation 1.15, and they equal to ($m_{eff} = m + m_a(\cot^2\theta + 1)/4$) and ($k_{eq} = k$). Notice that the effective mass of the system can be much larger than m if θ is small.

The resonance and antiresonance frequencies are given in Equation 1.16 and Equation 1.17, respectively. Transmissibility of the lumped model can be calculated with respect to resonance and antiresonance frequencies.

$$\omega_p = \sqrt{\frac{k}{m + m_a(\cot^2\theta + 1)/4}} \tag{1.16}$$

$$\omega_z = \sqrt{\frac{k}{m_a(\cot^2\theta - 1)/4}} \tag{1.17}$$

Then, transmissibility of the structure is

$$TR(\omega) = \frac{1 - (\frac{\omega}{\omega_z})^2}{1 - (\frac{\omega}{\omega_p})^2} \tag{1.18}$$

At large frequencies ($\omega >> \omega_{z1}$), transmissibility equation can be simplified as

$$TR_\infty = \left(\frac{\omega_p}{\omega_z}\right)^2 = \frac{m_a(\cot^2\theta - 1)}{4m + m_a(\cot^2\theta + 1)} \tag{1.19}$$

The frequency range where $TR(\omega) < 1$ is defined as stop band (phononic) gap. Besides, the depth of the band gap is important factor which determines the amount of transmitted vibration. Transmissibility of the mechanism is examined in Section 3.

When the band structure of the 1D array is considered, it can be said that band structure is strongly related by the motions of the neighbour unit cells. Using Bloch's theorem, equation of motion of the unit cell shown in the Figure 1.7(a) can be written as

$$\left((m + m_a) + \frac{m_a}{4}(\cot^2\theta - 1)(2 - e^{(i\gamma)} - e^{(-i\gamma)})\right)\ddot{x}_i + k(2 - e^{(i\gamma)} - e^{(-i\gamma)}) = 0 \tag{1.20}$$

Equation 1.20 is solved for γ between 0 and π with different mass ratios ($\mu = m_a/(m_a + m)$) and angles (θ). Band structure plots can be seen in Figure 1.8. Here, k taken as 1 N/m, $m + m_a$ =0.2 kg. With these parameters, the total mass and stiffness of the unit cell is the same when compared to the previous two unit cells. Band structure plot shows that inertial amplification system has a semi-infinite band gap, and band gap starting frequency can be reduced by decreasing angle θ or reducing mass m.

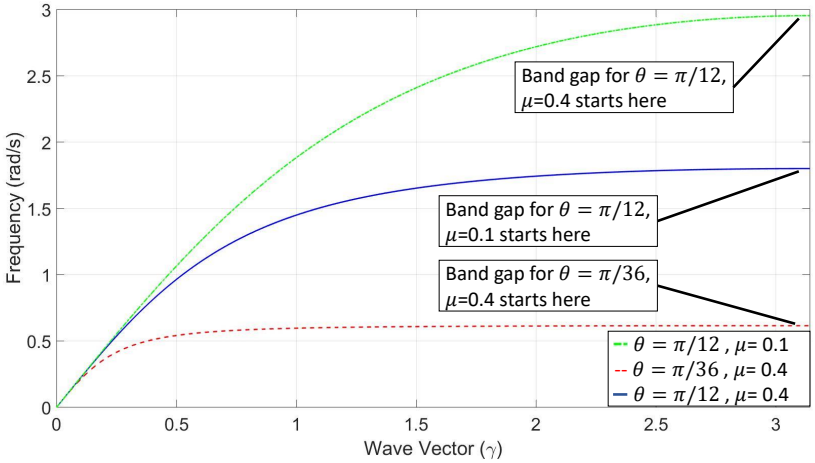

Figure 1.8. Band Structure Plot of 1D Array of Inertial Amplification Mechanism.

1.3. Motivation and Research Objective

In this thesis, inertial amplification mechanism is used in an axial to rotary motion conversion mechanism to obtain a wide and deep phononic band gap. Phononic band gap of the structure is increased without increasing the overall mass or decreasing the overall stiffness. Thus, vibration isolation is achieved in wide frequency ranges. Motivations behind the research can be summarized as

- In the literature, inertial amplification method is used with bridge type mechanisms or lever mechanisms. Using axial to rotary motion conversion mechanisms with inertial amplification method is a newly introduced concept.

- For the first time, inertial amplification method is used in novel axial to rotary motion mechanisms to lower the band gap frequency range.

- Wave propagation through the medium is eliminated in certain range of frequencies where the phononic band gap occurs. Consequently, the mechanism can be used as a vibration isolator or frequency filter.

- To achieve a wide phononic band gap at low frequencies for axial excitations,

the first vibration mode has to be axial-torsional coupled mode and the second vibration mode should be at a much higher frequency than the first one. For this reason, one of the aims of thesis is to minimize the frequency ratio of first two natural frequencies ($\omega_1/\omega_2 < 0.3$). Design of a mechanism according to their mode shapes and natural frequency ratio is the major challenge of this thesis.

2. LINEAR-TO-ANGULAR-DISPLACEMENT-DEVICE-MECHANISM

In literature review, it can be seen that LADD (see in Figure 2.1) is a suitable motion conversion mechanism for inertial amplification due to its frictionless design. Besides, axial to rotary motion conversion can be used as an alternative approach for the use of inertial amplification mechanisms [56, 57]. In this device, when the bottom ring is excited, helical wires create both rotational and translational motion in the upper ring (see Figure 2.1(a)). The motion is transmitted to the upper cells with the same principle in periodic structure as it can be seen from Figure 2.1(b). To obtain wide phononic band gap in LADD mechanism, effective inertia of the system has to be increased, which requires the maximization of the rotational motion of the rings from unit input translational motion. Besides, bending stiffness of the structure has to be increased to achieve higher upper band gap limit. However, the amount of rotation is limited in LADD mechanism, which is important for effective inertia of the systems, and bending natural frequencies has to be increased to maximize the band gap. Therefore, helical wire theory is examined to overcome these problems.

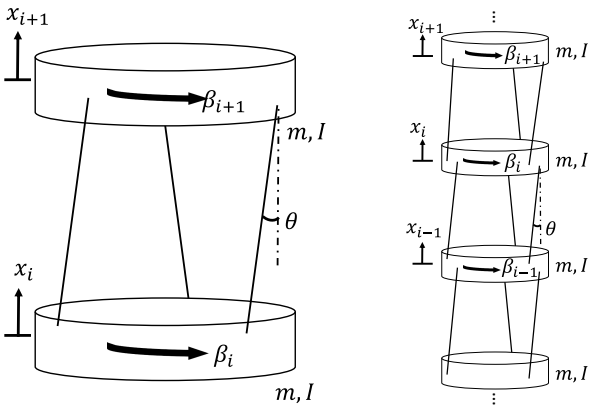

(a) (b)

Figure 2.1. Unit Cell and Periodic Structure of the LADD Mechanism, (a) Unit Cell, (b) Lumped Parameter Model.

2.1. Helical Wires

To maximize the rotation of the rings and increase the stiffness of the structure, helical wire theory is studied. First, deflection-rotation relationship of the helical wires are examined with respect to several theories. Then, natural frequencies of the wires are calculated via beam theory. Finally, the models are validated with experiments. After the validation, optimization process is conducted to maximize the phononic band gap of the structure.

2.1.1. Large Deflections in Helical Wires

In the literature, various spring parameters are investigated to find the amount of rotation of helical spring from unit axial movement. Number of active coils (n), spring diameter (d), helix angle (α), pitch (p), wire cross sectional shape and material properties of spring (Elastic modulus (E), poisson ratio (v), shear modulus (G), density (ρ)) are some of the important parameters for helical spring design (see Figure 2.2).

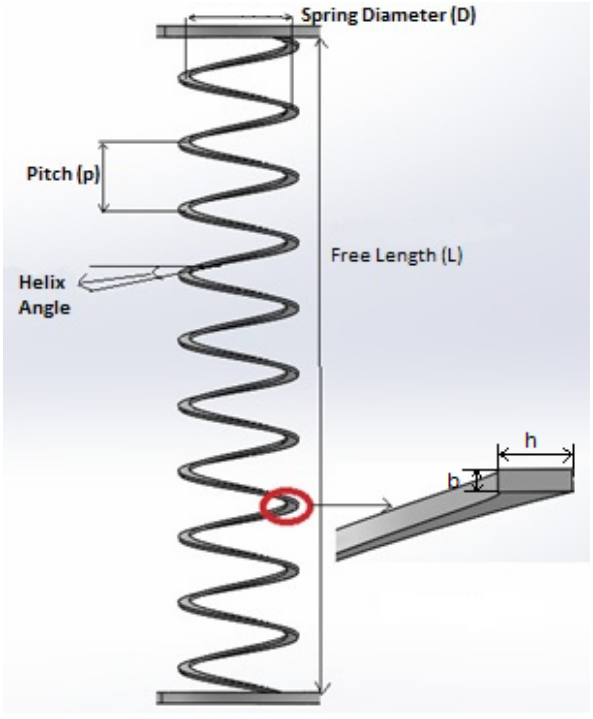

Figure 2.2. Some Important Parameters of Helical Springs. The Example Wire Cross Sectional Shape Zoomed at the Right Side.

Force and moment equilibrium equations of the helical springs are represented in detail by Love [58]. It is assumed that wire or rod is naturally straight at the beginning. Then, it is finitely bent and twisted, and held in its new state with certain forces and couples. Equilibrium equations consist of moving axes of x, y and z. Components of curvature and twist are equal to κ, λ and τ with respect to x, y and z axes (see Figure 2.3). In Figure 2.3, P has been taken as a normal point and P' is a different point, which has small displacement ds away from P [59].

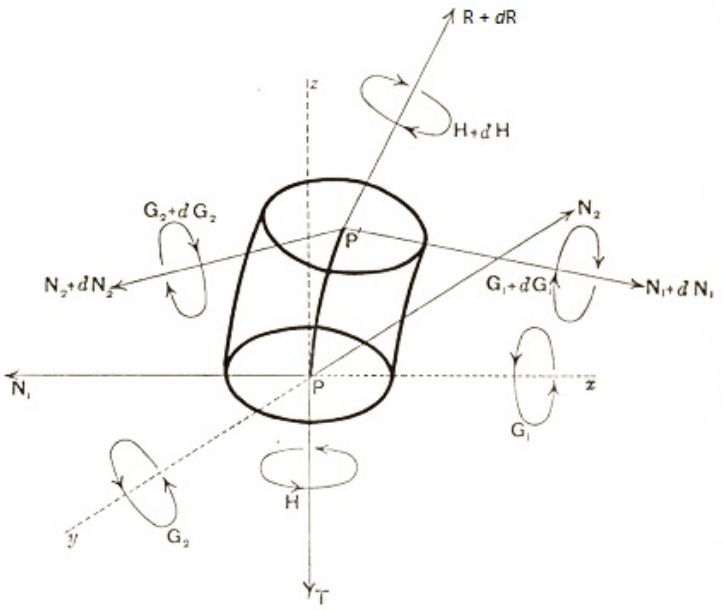

Figure 2.3. Representation of Forces and Couples on Helical Wire.

N_1 and N_2 are components of shear force and R is the tension at any point. G_1, G_2 are the flexural couples and H is the torsional couple. The external forces that effect the system are taken as X, Y and Z, and the external couples that effect the system are taken as L, M and N respectively. According to these variables, Love [58] found the expressions below.

$$\frac{dN_1}{ds} - N_2\tau + R\lambda + X = 0 \tag{2.1}$$

$$\frac{dN_2}{ds} - R\kappa + N_1\tau + Y = 0 \tag{2.2}$$

$$\frac{dR}{ds} - N_1\lambda + N_2\kappa + Z = 0 \tag{2.3}$$

$$\frac{dG_1}{ds} - G_2\tau + H\lambda - N_2 + L = 0 \tag{2.4}$$

$$\frac{dG_2}{ds} - H\kappa + G_1\tau + N_1 + M = 0 \tag{2.5}$$

$$\frac{dH}{ds} - G_1\lambda + G_2\kappa + N = 0 \tag{2.6}$$

Now, there are 6 equations and 9 unknown quantities ($N_1, N_2, R, G_1, G_2, H, \kappa, \lambda$ and τ). To reduce the unknown number Love used "Bernoulli-Eulerian Theory" which explains the relation between stress couples and curvature-twist [58].

$$G_1 = EI_1\kappa \tag{2.7}$$

$$G_2 = EI_2\lambda \tag{2.8}$$

$$H = GI_p\tau \tag{2.9}$$

where I_1 and I_2 is the area moment of inertia of the wire cross section, and I_p is the polar moment of the wire cross section.

To solve the Love's equation set, Wahl [59] used simple assumptions. The first one is that the helical spring is axially loaded with the ends free to rotate as the spring deflects Figure 2.4(a). Besides, the length of the wire does not change, which means that axial strain values are neglected. After that, it is assumed that $I_1 = I_2$. As a

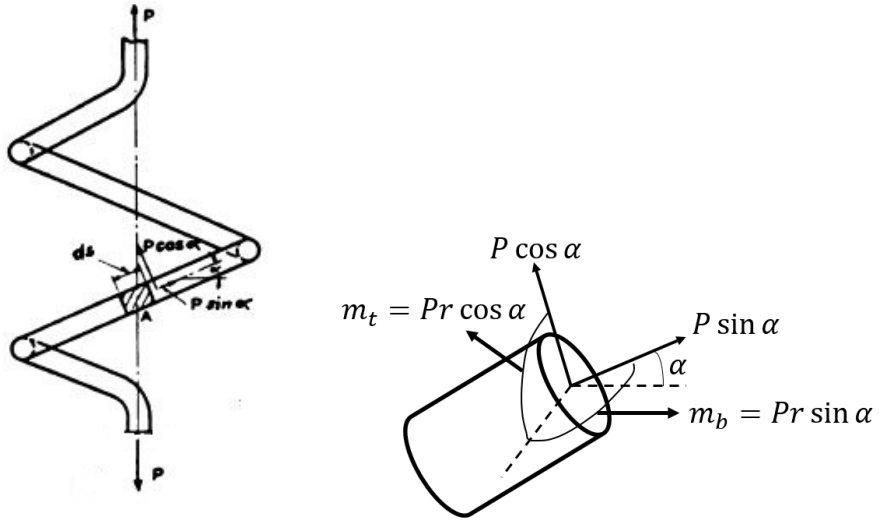

(a) (b)

Figure 2.4. Force Distribution in Helical Spring According to Wahl, (a) Axially Loaded Spring [59], (b) Distribution of Applied Loads and Moments in Wire Cross-section.

result, forces and couples can be expressed like in Figure 2.4(b). Curvature change and stress couples can be expressed easily after this point. Initial helix angle is given as α_0 and final helix angle is given as α. Similarly, initial spring radius is given as r_0 and final coil radius is given as r. Curvature change of wire when the spring deflects from α_0 to α will be equal to

$$\Delta\alpha = \frac{\cos^2\alpha}{r} - \frac{\cos^2\alpha_0}{r_0} \tag{2.10}$$

Change in the curvature is the result of bending moment (m_b) which is equal to

$$m_b = Pr\sin\alpha \tag{2.11}$$

Bending moment should be equal to the flexural rigidity EI multiplied by the curvature change $\Delta\alpha$ [58]. Finally, it is found that

$$Pr\sin\alpha = EI\left(\frac{\cos^2\alpha}{r} - \frac{\cos^2\alpha_0}{r_0}\right) \tag{2.12}$$

Twist in wire per unit length can be found from the elastic theory similarly [59].

$$\Delta\theta = \frac{\sin\alpha\cos\alpha}{r} - \frac{\sin\alpha_0\cos\alpha_0}{r_0} \tag{2.13}$$

When this is multiplied with torsional rigidity GI_p, results will give the twisting moment m_t [58].

$$Pr\cos\alpha = GI_p\left(\frac{\sin\alpha\cos\alpha}{r} - \frac{\sin\alpha_0\cos\alpha_0}{r_0}\right) \tag{2.14}$$

If Equation 2.12 and Equation 2.14 are solved together, final mean radius will be found in terms of material properties (E, G), geometrical properties of wire cross section (I, I_p), final helix angle (α) and initial parameters of the helical spring (α_0, r_0).

$$r = \frac{\cos^2\alpha}{\cos^2\alpha_0}\left(\frac{\tan^2\alpha - \frac{EI}{GI_p}}{\tan\alpha\tan\alpha_0 - \frac{EI}{GI_p}}\right) \tag{2.15}$$

Therefore, numerical solution of the system will be possible. Final spring radius can be obtained easily by only changing the final helix angle. Deflection and rotation values of the spring can be found after that Figure 2.5.

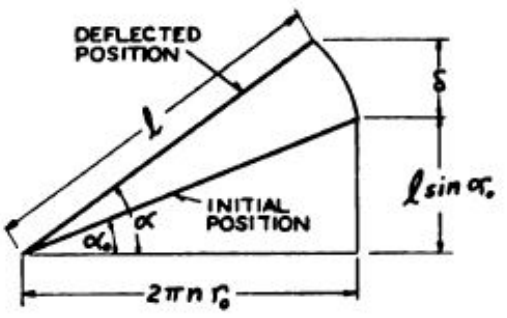

Figure 2.5. Spring Length Change with Large Helix Angle [59].

Deflection and rotation can be calculated from the geometrical properties of the triangles (Figure 2.5).

$$\delta = \frac{2\pi n r_0}{\cos\alpha_0}(\sin\alpha - \sin\alpha_0) \tag{2.16}$$

where, n=number of active coils and δ=deflection of the spring.

$$\beta = \frac{2\pi n r_0}{\cos\alpha_0}\left(\frac{\cos\alpha}{r} - \frac{\cos\alpha_0}{r_0}\right) \tag{2.17}$$

where, β is the angle of rotation and expressed in radians. Witz [60] also used Love's equations with axial strain effects have been taken into account, differing from Wahl [59]. The derived equations (Equations 2.18, Equations 2.19 and Equations 2.20) are used for flexible marine cables which have helical structures like springs. This formulation can be extended to helical springs. The deflection and rotation effects can be observed from Figure 2.6.

$$\epsilon_x = \frac{\sin\alpha}{\sin\alpha_0}\left(1 + \frac{P\sin\alpha_0}{EA}\right) - 1 \tag{2.18}$$

$$\Delta L = \epsilon_x L \tag{2.19}$$

$$\tan\alpha = \tan\alpha_0 \frac{(1+\epsilon_x)}{1 - \frac{\Delta r}{r} + \frac{\beta L}{2\pi}} \tag{2.20}$$

When the equations of Witz [60] are iteratively solved, deflection-rotation relation can be found easily. Phillips and Costello [61] have used the same assumptions with Wahl [59] except that they include the change of the length of the wire, like Witz [60]. Therefore, axial strain values of the wire can be calculated in this method. Phillips and Costello assumed that external force P and torque T_s are applied at the end of the springs. The equilibrium equations for P and T_s can be expressed as

$$\frac{Pr_0^2}{EI} = \frac{r_0}{r}\frac{\cos\alpha}{1+v}\left(\frac{r_0}{r}\sin\alpha\cos\alpha - \sin\alpha_0\cos\alpha_0\right) - \frac{r_0}{r}\sin\alpha\left(\frac{r_0}{r}\cos^2\alpha - \cos^2\alpha_0\right) \tag{2.21}$$

$$\frac{T_s r}{EI} = \frac{\sin\alpha}{1+v}\left(\frac{r_0}{r}\sin\alpha\cos\alpha - \sin\alpha_0\cos\alpha_0\right) + \cos\alpha\left(\frac{r_0}{r}\cos^2\alpha - \cos^2\alpha_0\right) \tag{2.22}$$

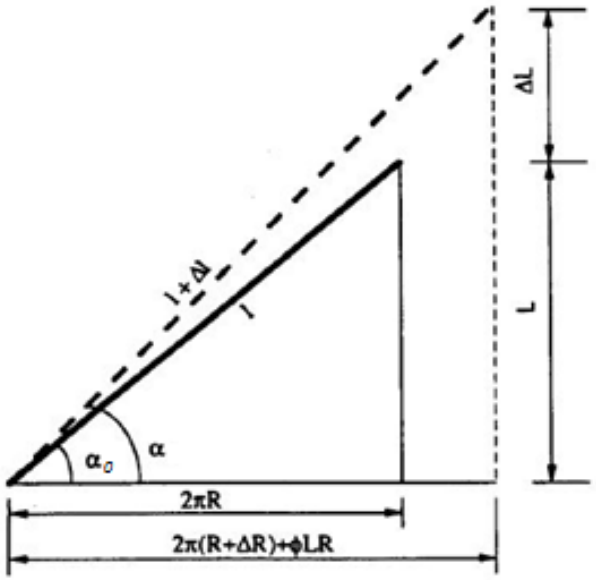

Figure 2.6. Spring Length Change with Large Helix Angle According to Witz [60].

These two equations can be solved with the symbolic toolbox of MATLAB.

Nagaya [62] have used three-dimensional curved beam theory to find the exact results of resultant forces in cross-section shapes like ellipse or rectangle. A local coordinate system has been used for this job. However, in this case, it is difficult to apply appropriate boundary conditions along the surface of the coil. Fourier expansion collocation method has been used for irregular boundaries [62]. Since the equations are complex, they are not mentioned here. As a result, displacements, angle of rotations, resultant forces and resultant moments are calculated for every point of the coil.

However, at this point, all formulations (except Nagaya) have been derived for the case where the flexural rigidities of the cross section are equal. Consequently, these formulas can be used in square and circular cross sections. So, these formulas may cause some amount of error with other cross section types, like rectangular or oval. However, it should be noted that the number of studies on this issue is limited. After the analytical modelling is completed, finite element method is applied to understand the deformation characteristics of system and results are compared to the analytical ones. Additionally, modal analysis is applied to determine natural frequencies and

mode shapes of the system with the help of the finite element method. The results are given in Section 2.2.

2.1.2. Vibrations of the Helical Wires

Beam element formulation is widely used in literature for several purposes. To calculate the natural frequency of the helical spring, stiffness and mass matrix of the structure formulated with beam element theory. Then, both matrices multiplied with rotation matrix to obtain a helical spring. Elastic beam element matrices of Dr. Przemieniecki [63], which is also utilized in the ANSYS Beam4 3D elastic beam element is used as stiffness matrices. However, to improve the accuracy of the results gravitational effects are also considered. For this reason, Dr. Yokoyoma's [64] gravitation stiffness matrix is superposed with element stiffness matrix. The stiffness and mass matrices are given below and their constants are given in Appendix A. Shear coefficients of the stiffness matrix are taken from literature [65].

In the Figure 2.7(a), an illustration of an used beam element and its coordinate system is shared. The selected beam element has 12 degree of freedom. The order of the degrees of freedom can be seen in Figure 2.7(b).

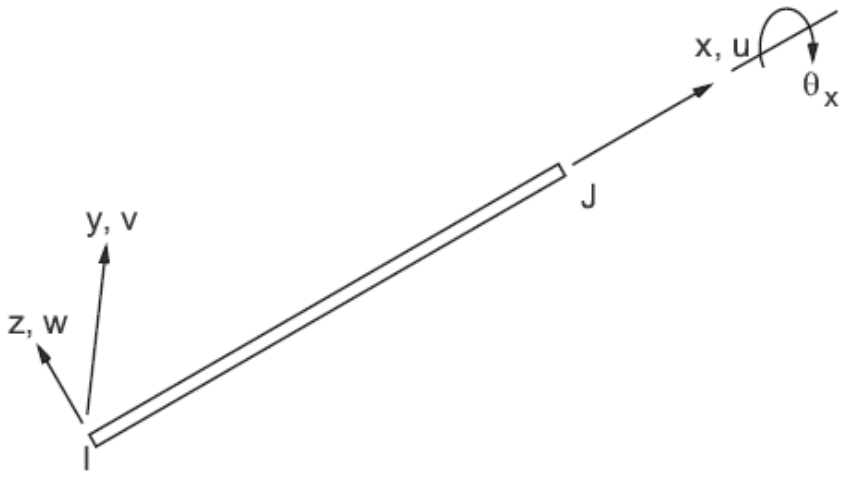

(a)

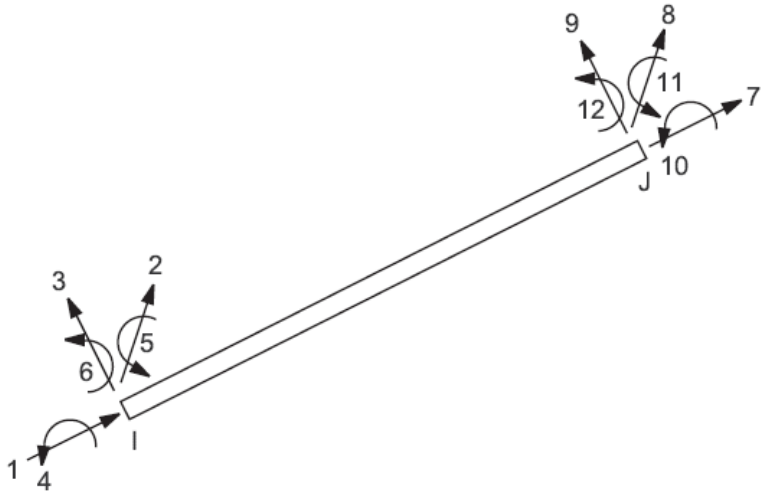

(b)

Figure 2.7. An Example Beam Element and Its Order of Degrees of Freedom, (a) Beam Element and Its Coordinate System, (b) Order of Degrees of Freedom.

Local element stiffness matrix of Dr. Przemieniecki is given in Equation 2.23.

$$[K_l] = \begin{bmatrix} \frac{AE}{L} & 0 & 0 & 0 & 0 & 0 & \frac{-AE}{L} & 0 & 0 & 0 & 0 & 0 \\ & a_z & 0 & 0 & 0 & c_z & 0 & -a_z & 0 & 0 & 0 & c_z \\ & & a_y & 0 & -c_y & 0 & 0 & 0 & -a_y & 0 & -c_y & 0 \\ \text{Sym.} & & & \frac{GJ}{L} & 0 & 0 & 0 & 0 & 0 & \frac{-GJ}{L} & 0 & 0 \\ & & & & e_y & 0 & 0 & 0 & c_y & 0 & f_y & 0 \\ & & & & & e_z & 0 & -c_z & 0 & 0 & 0 & f_z \\ & & & & & & \frac{AE}{L} & 0 & 0 & 0 & 0 & 0 \\ & & & & & & & a_z & 0 & 0 & 0 & -c_z \\ & & & & & & & & a_y & 0 & c_y & 0 \\ & & & & & & & & & \frac{GJ}{L} & 0 & 0 \\ & & & & & & & & & & e_y & 0 \\ & & & & & & & & & & & e_z \end{bmatrix} \tag{2.23}$$

Local gravity element stiffness matrix of Dr. Yokoyoma is given in Equation 2.24.

$$[K_g] = \rho A g \begin{bmatrix} 0 & 0 & 0 & 0 & 0 & 0 & 0 & 0 & 0 & 0 & 0 & 0 \\ & A_{11} & 0 & 0 & 0 & A_{12} & 0 & A_{13} & 0 & 0 & 0 & A_{14} \\ & & B_{11} & 0 & B_{12} & 0 & 0 & 0 & B_{13} & 0 & B_{14} & 0 \\ \text{Sym.} & & & 0 & 0 & 0 & 0 & 0 & 0 & 0 & 0 & 0 \\ & & & & A_{22} & 0 & 0 & 0 & A_{23} & 0 & 0 & A_{24} \\ & & & & & B_{22} & 0 & 0 & B_{23} & 0 & B_{24} & 0 \\ & & & & & & 0 & 0 & 0 & 0 & 0 & 0 \\ & & & & & & & A_{33} & 0 & 0 & 0 & A_{34} \\ & & & & & & & & B_{33} & 0 & B_{34} & 0 \\ & & & & & & & & & 0 & 0 & 0 \\ & & & & & & & & & & A_{44} & 0 \\ & & & & & & & & & & & B_{44} \end{bmatrix} \tag{2.24}$$

The total local element stiffness matrix is the sum of Equation 2.23 and Equation 2.24. Local element mass matrix is given in Equation 2.25.

$$[M_l] = M_t \begin{bmatrix} \frac{1}{3} & 0 & 0 & 0 & 0 & 0 & \frac{1}{6} & 0 & 0 & 0 & 0 & 0 \\ & A_z & 0 & 0 & 0 & C_z & 0 & B_z & 0 & 0 & 0 & -D_z \\ & & A_y & 0 & -C_y & 0 & 0 & 0 & B_y & 0 & D_y & 0 \\ \text{Sym.} & & & \frac{J_x}{3A} & 0 & 0 & 0 & 0 & 0 & \frac{J_x}{6A} & 0 & 0 \\ & & & & E_y & 0 & 0 & 0 & -D_y & 0 & F_y & 0 \\ & & & & & E_z & 0 & D_z & 0 & 0 & 0 & F_z \\ & & & & & & \frac{1}{3} & 0 & 0 & 0 & 0 & 0 \\ & & & & & & & A_z & 0 & 0 & 0 & -C_z \\ & & & & & & & & A_y & 0 & C_y & 0 \\ & & & & & & & & & \frac{J_x}{3A} & 0 & 0 \\ & & & & & & & & & & E_y & 0 \\ & & & & & & & & & & & E_z \end{bmatrix} \tag{2.25}$$

The overall stiffness and mass of the beam element matrices are 12×12. The matrices are include the effect of axial strains ($[K_l]$) and gravity based deformations ($[K_g]$). However, to convert beams into a helical spring a rotation matrix is required. Rotation matrix for global cartesian coordinate transformation can be expressed as

$$[\Phi] = \begin{bmatrix} \phi & 0 & 0 & 0 \\ & \phi & 0 & 0 \\ & & \phi & 0 \\ \text{Sym.} & & & \phi \end{bmatrix} \tag{2.26}$$

where ϕ is derived from Serret-Frenet equations [66] which can be written as

$$[\phi] = \begin{bmatrix} \frac{(\tau^2+\kappa^2\cos(\psi s))}{\psi^2} & \frac{\kappa\sin(\psi s)}{\psi} & \frac{\kappa\tau(1-\cos(\psi s))}{\psi^2} \\ \frac{\kappa\sin(\psi s)}{\psi} & -\cos(\psi s) & \frac{-\tau\sin(\psi s)}{\psi} \\ \frac{\kappa\tau(1-\cos(\psi s))}{\psi^2} & \frac{-\tau\sin(\psi s)}{\psi} & \frac{(\kappa^2+\tau^2\cos(\psi s))}{\psi^2} \end{bmatrix} \tag{2.27}$$

where $\psi = \sqrt{\tau^2 + \kappa^2}$ and s is the arc coordinate. The variables of the Equation 2.27 is shared in Appendix A.

2.2. Validation of Helical Wires Deflection and Vibration Models

For validation of the analytical models, finite element models are created. Moreover, experiments are conducted to see the accuracy of the models. Two prototypes are designed with the properties given in Table 2.1, shown in Figure 2.2. A pair of springs with different hands (right handed and left handed) are connected as in Figure 2.8. Both ends of the Specimen 1 (see Figure 2.8(a)) and Specimen 2 (see Figure 2.8(b)) are extended by 10.5 cm and 7.5 cm, respectively. The mean radii obtained from these experiments are compared with the ones found from the analytical models. The result of the experiment and analytical models are given in Table 2.2. The material of the spring is steel (E=200 GPa, ρ=7800 kg/m^3, μ=0.3). To calculate the mean radius in FEM, 2 nodes have been taken inside of each coil that the distance between them are giving the diameter of the helix. Then, the averages of their radius change have been

calculated to reach the results. For FEM modeling, commercial software, ABAQUS, is used. The structure is globally seeded with 0.08 mm edge size elements. 10 node quadratic tetrahedron elements are used.

Table 2.1. Properties of the Designed Springs with Rectangular Cross-Section.

Spring Properties	**Specimen 1**	**Specimen 2**
Pitch (p) (mm)	92.8	25
Mean radius (r) (mm)	26	13.5
b (mm)	0.66	0.3
h (mm)	2.6	1.2
n (turns)	3.5	6

Table 2.2. Results of Mean Radius After Deflection According to Different Approaches.

Models	**Specimen 1 (mm)**	**Specimen 2 (mm)**
Wahl [59]	19.0	11.7
Witz [60]	22.4	9.6
Phillips-Costello [61]	22.5	12.7
Nagaya [62]	24.2	11.0
ABAQUS	22.8	12.4
Experiment	22.8	11.1

According to the results, it can be said that FEM (ABAQUS) and Phillips-Costello theory give the best results for Specimen 1. For Specimen 2, Nagaya's theory give the best results. Analytical models, which explained deflection and rotation relationship, have good correlations with experiments for both specimens. The results show that analytical models can be used in the optimization process to maximize the rotation from the unit deflection. However, to maximize the phononic band gap of the structure, vibrations of the helical wires have to be verified with experiments. Then, verified vibration models are integrated into the optimization model.

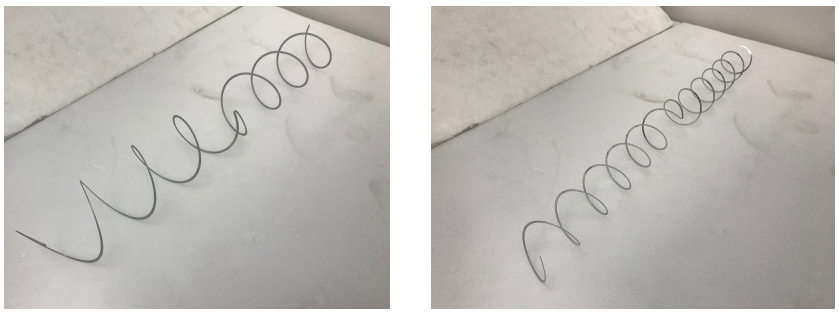

(a) (b)

Figure 2.8. Double-Handed Helical Springs, (a) Specimen 1 with 3.5 Turns on Each Side, (b) Specimen 2 with 6 Turns on Each Side.

To model the natural frequencies, finite element models are created with solid and beam elements. Notice that beam elements of ABAQUS can only generate 2D beam structures but 3D model of the helical spring is created with Python scripts. For the band gap maximization, all three models can be used, but solid FEM models require much more time than the beam element models. Moreover, ABAQUS beam element model solution time is almost two times higher than the analytical model. In Figure 2.9, the first mode shape of the Specimen 2 is shared considering 3 different analysis methods. For experimental validation process of the vibration models, Specimen 2 is selected due to its dimensions. During the experiment, Specimen 2 is fixed at both ends. Laser Doppler Vibrometer is used to measure vibration velocity, and specimen is excited with an impact hammer. The average of 60 measurements are taken to decrease noise effect in the system. The results of the experiment and models can be seen in Table 2.3. The frequency response plot of the Specimen 2 can be seen in Figure 2.10.

Experiments and models have good correlation for Specimen 2. The analytical model gives more accurate results, and ABAQUS beam element model results are better than solid element model. However, cross section of the wires can be taken as an optimization variable to increase the bending stiffness and phononic band gap of the structure. Therefore, experiments are conducted with additional new specimen, Specimen 3. Apart from Specimen 1 and 2, Specimen 3 has an trapezoidal cross section (see Figure 2.11(a)), and its cross sectional area is much larger. The design variables of the Specimen 3 can be seen in Table 2.4.

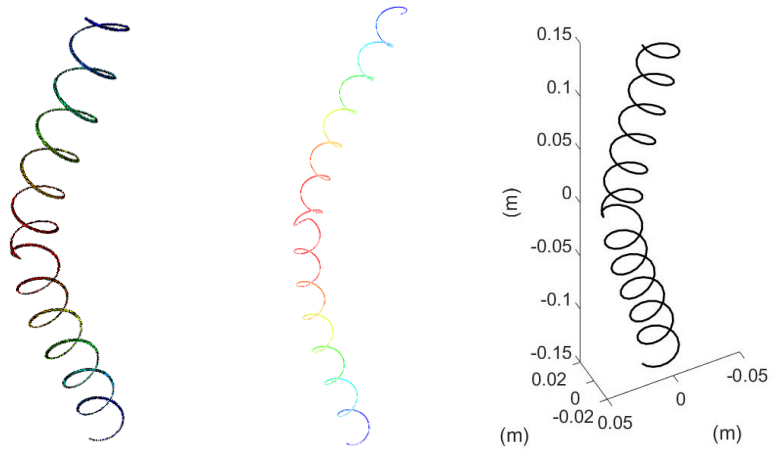

(a) (b) (c)

Figure 2.9. Different Computational Models for Specimen 2, (a) ABAQUS Solid Model (6.0 Hz), (b) ABAQUS Beam Model (5.3 Hz), (c) Analytical Model (5.3 Hz).

Table 2.3. Natural Frequencies of Specimen 2 According to Different Approaches.

Mode Shape	**Experiment (Hz)**	**ABAQUS Solid Model (Hz)**	**ABAQUS Beam Model (Hz)**	**Analytical Model (Hz)**
Mode-1 (Bending)	5.0	6.0	5.3	5.3
Mode-2 (Bending)	5.0	6.0	5.3	5.3
Mode-3 (Bending)	12.8	15.4	14.7	14.2
Mode-4 (Bending)	13.0	15.6	14.7	14.6
Mode-5 (Axial-Torsional)	23.8	18.8	22.1	18.4

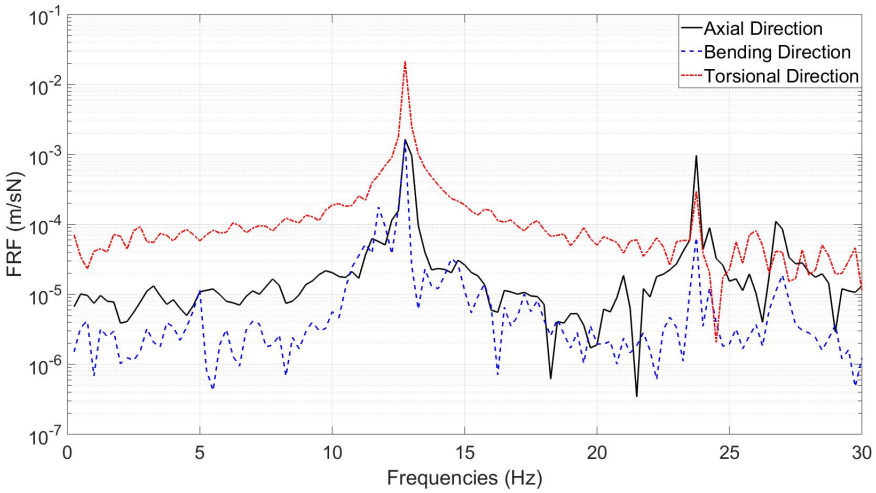

Figure 2.10. Frequency Response Plot of Specimen 2 Excited along Axial, Bending and Torsional Directions, Respectively.

Table 2.4. Properties of the Designed Springs with Trapezoidal Cross-Section.

Spring Properties	**Specimen 3**
Pitch (p) (mm)	70
Outer Diameter (d_o) (mm)	64
b_1 (mm)	3.5
b_2 (mm)	2.8
h (mm)	19
n (turns)	4

During the experiment, Specimen 3 is hung by rubber cords. Free-free boundary condition is used to examine the accuracy of the models. It is excited via an impact hammer and acceleration is measured with a 3D accelerometer. For Specimen 3, 3D accelerometer can be used instead of Laser Doppler Vibrometer because Specimen 2 does not have enough cross sectional area to connect an accelerometer.

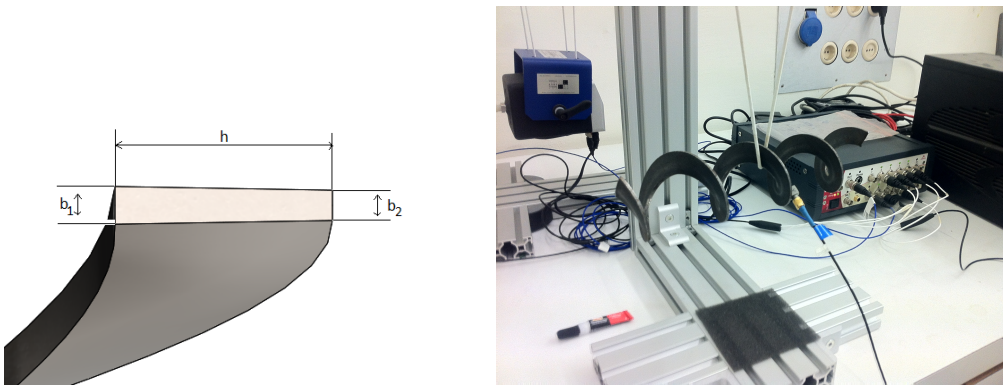

(a) (b)

Figure 2.11. Cross-Section of the Helical Wire and Experimental Setup of Specimen 3, (a) Cross-Section, (b) Experimental Setup.

The mode shapes of Specimen 3 for all three models can be seen in Figure 2.12. The first mode shape is in the bending direction. The results and frequency response plot of the spring can be seen in Table 2.5 and Figure 2.13, respectively.

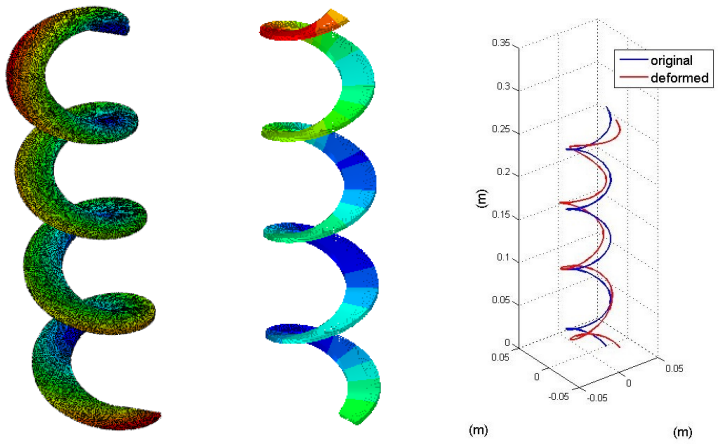

(a) (b) (c)

Figure 2.12. Different Computational Models for Specimen 3, (a) ABAQUS Solid Model (90.9 Hz), (b) ABAQUS Beam Model (96.6 Hz), (c) Analytical Model (97.4 Hz).

Table 2.5. Natural Frequencies of Specimen 3 According to Different Approaches.

Mode Shape	**Experiment (Hz)**	**ABAQUS Solid Model (Hz)**	**ABAQUS Beam Model (Hz)**	**Analytical Model (Hz)**
Mode-1 (Bending)	92.0	90.9	96.6	97.4
Mode-2 (Bending)	92.0	90.9	96.6	97.8
Mode-3 (Axial-Torsional)	201.3	197.5	182.2	183.8
Mode-4 (Bending)	228.8	224.0	233.4	238.8
Mode-5 (Bending)	228.8	225.2	239.6	239.3

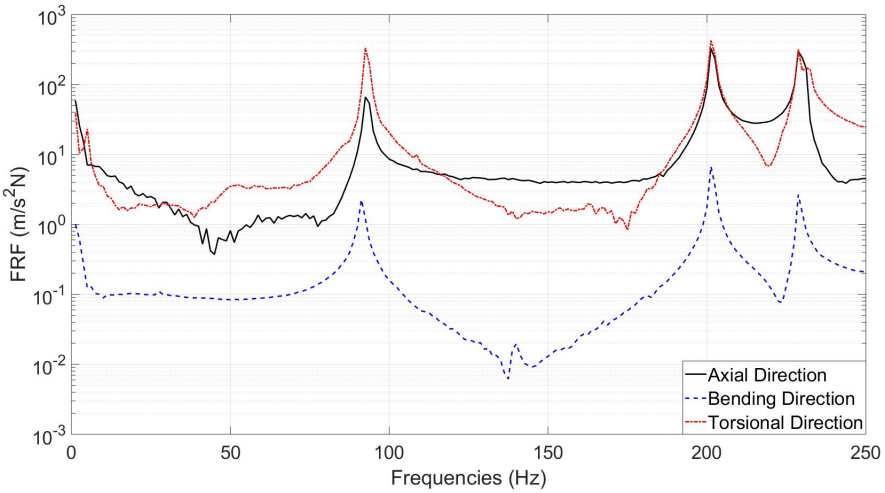

Figure 2.13. Frequency Response Plot of Specimen 3 Excited along Axial, Bending and Torsional Directions, Respectively.

Table 2.5 shows that solid elements give more accurate results for Specimen 3. Additionally, ABAQUS beam element results are very similar to analytical model. However, in order to maximize band gap, helical springs should be integrated into disks as in LADD mechanism. For this reason, a prototype (see Figure 2.14(a)) is created and tested. In the prototype, two helical wires which have identically same properties with Specimen 3 are used. Besides, FE model of the prototype is created with solid elements. The results and mode shapes can be seen in Table 2.6 and Figure 2.14. The transmissibility plot of the prototype can be seen in Figure 2.15.

Table 2.6. Natural Frequencies of Specimen 3 According to Different Approaches.

Mode Shape	**Experiment (Hz)**	**ABAQUS Solid Model (Hz)**
Mode-1 (Bending)	43.8	44.8
Mode-2 (Bending)	43.8	44.8
Mode-3 (Axial-Torsional)	85.0	95.0
Mode-4 (Bending)	93.0	95.9
Mode-5 (Bending)	95.6	96.1

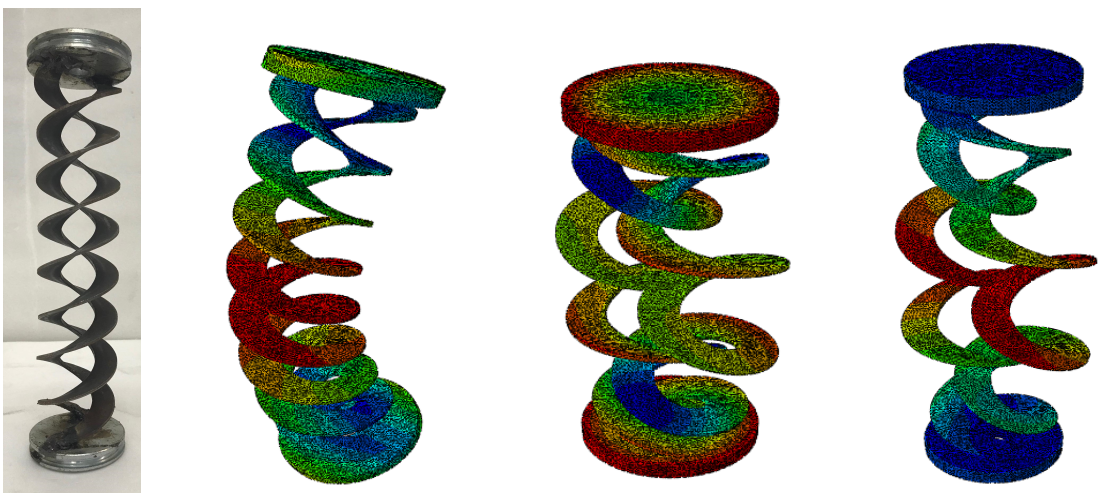

(a) (b) (c) (d)

Figure 2.14. LADD Mechanism with Double Helical Spring and Its Mode Shapes, (a) LADD Mechanism with Double Helical Spring, (b) First Mode Shape (44.8 Hz), (c) Third Mode Shape (95.0 Hz), (d) Fourth Mode Shape (95.9 Hz).

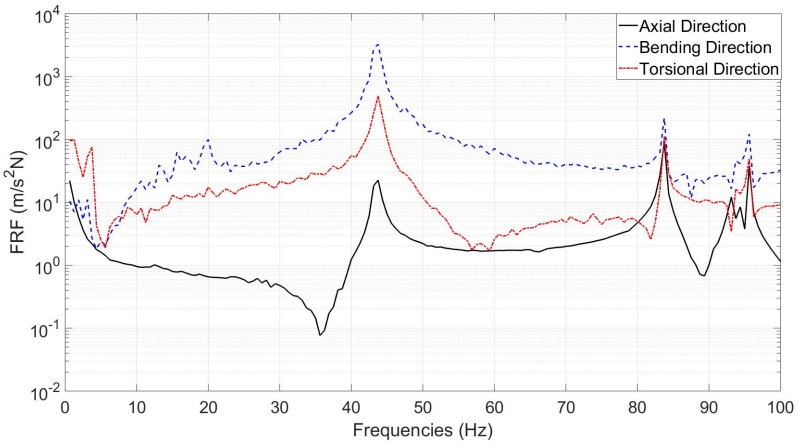

Figure 2.15. Frequency Response Plot of the Prototype with Two Helical Springs and Disks Excited along Axial, Bending and Torsional Directions, Respectively.

The results of the FE model have a good correlation with experiments. The error of third natural frequency, which is axial-torsional coupling mode originate from the welding misalignments and assembly problems.

In the prototype, third natural frequency has axial-torsional coupling mode (see Figure 2.14(c)), and others have bending mode (see Figure 2.14(b) and Figure 2.14(d)). As it is mentioned before, axial-torsional coupling mode is important for inertial amplification method, and it should be the first natural frequency for band gap maximization. At this point, inertial amplification models are created with beam elements, and solid elements are used as reference due to their high accuracy. With inertial amplification models, natural frequencies of the mechanism will be analysed to maximize the band gap, and the axial-torsional coupling natural frequency will be tried to be reduced until it becomes the first natural frequency.

2.3. Inertial Amplification Model

For band gap maximization, inertial amplification models are created as it can be seen in Figure 2.16. In these models, the disks are modelled as straight beams and their free ends are only allowed to rotate and translate in y direction. The inertia and density of this beam is different from the rest of the spring and it is much stiffer ($E = 20500$ GPa) and heavier ($\rho = 312000$ kg/m^3). The results of an example case are shared in Table 2.7.

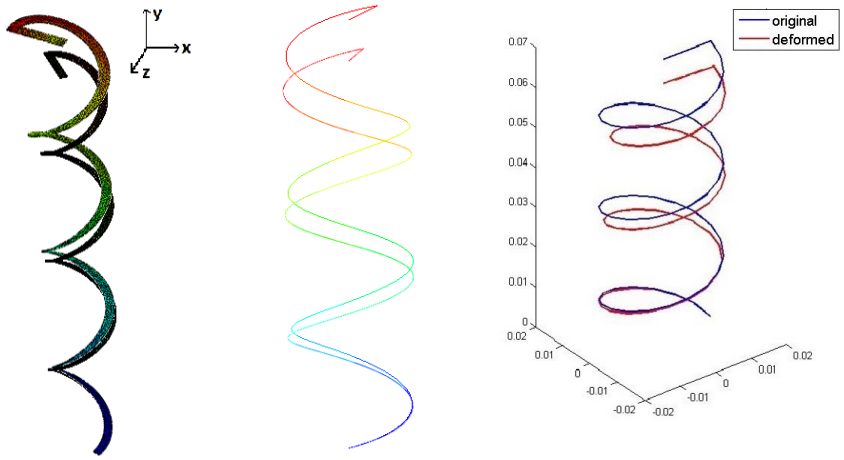

(a) (b) (c)

Figure 2.16. Different Computational Models of Inertial Amplification Mechanism, (a) ABAQUS Solid Model (22.6 Hz), (b) ABAQUS Beam Model (23.2 Hz), (c) Analytical Model (23.9 Hz).

Table 2.7. Natural Frequencies of Inertial Amplification Mechanism According to Different Approaches. Here, pitch=23 mm, outer-diameter=30 mm, cross section=2-0.5 mm

Mode Shape	**ABAQUS Solid Model (Hz)**	**ABAQUS Beam Model (Hz)**	**Analytical Model (Hz)**
Mode-1 (Axial-Torsional)	22.6	23.2	23.9
Mode-2 (Bending)	102.3	101.7	96.0
Mode-3 (Bending)	109.4	117.7	101.9
Mode-4 (Bending)	119.4	120.6	125.8
Mode-5 (Bending)	135.2	135.8	146.3

Table 2.7 shows that beam element models give similar results with solid models. The inertial amplification model can be used for optimization process to maximize the phononic band gap.

2.4. Prestressesed Helical Wires

In spring models, prestress can also be used as a design parameter for band gap maximization. Prestressed helical wires have high bending natural frequencies and low axial-torsional coupling natural frequency. In Table 2.8, results show that bending natural frequency can be increased when the helical wires are stretched. Transmissibility plot of Specimen 2 with and without stretching can be seen in Figure 2.17.

As it can be seen from the Table 2.8 and Figure 2.17, the bending natural frequencies can be increased by applying tensile prestress. In ABAQUS solid and beam models, deflection can be defined as a parameter which increases the solution time excessively. Besides, in analytical models modelling deflection and calculating natural frequencies of deflected body is a complex task. For this reason, gravity is used as a prestress parameter instead of deflection. The increasing gravity increases the deflection of the spring, which can be easily modelled. In Table 2.8, gravity is increased until 20 cm deflection is reached. Then, according to determined gravity value, natural frequencies are calculated, and they indicate good correlations for all models. However, to determine the amount of gravity, maximum stress of the springs should be examined, and gravity is selected without causing static or fatigue failure.

The errors are originated from the loading condition differences (see Figure 2.18(a) and Figure 2.18(b)), which lead to change the stress and displacement distributions. The effect of tip and gravity based loading on displacements can be seen in Figure 2.18(c) and Figure 2.18(d) for an example case. However, error rates are in acceptable rates which are less than 10 percent.

Table 2.8. Natural Frequencies of Specimen 2 When It is Stretched 20 cm.

Mode Shape	**Experiment (Untensioned) (Hz)**	**Experiment (Tensioned) (Hz)**	**ABAQUS Solid Model (Tensioned) (Hz)**	**ABAQUS Beam Model (Tensioned) (Hz)**	**Analytical Model (Tensioned) (Hz)**
Mode-1 (Bending)	5.00	9.75	10.09	9.79	9.93
Mode-2 (Bending)	5.00	9.75	10.23	9.91	10.01
Mode-3 (Bending)	12.75	19.5	20.86	20.26	23.06
Mode-4 (Bending)	13.00	20.25	21.11	20.68	24.20
Mode-5 (Axial-Torsional)	23.75	21.50	23.97	23.55	24.71

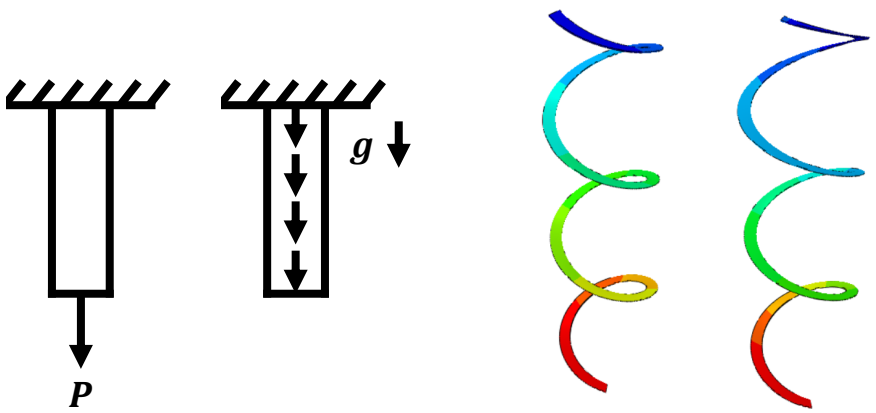

(a) (b) (c) (d)

Figure 2.18. Load and Displacement Distributions of (a) Load at Tip (b) Gravity Based Distributed Load (c) Gravity Load Case Displacements, (d) Tip Load Case Displacements.

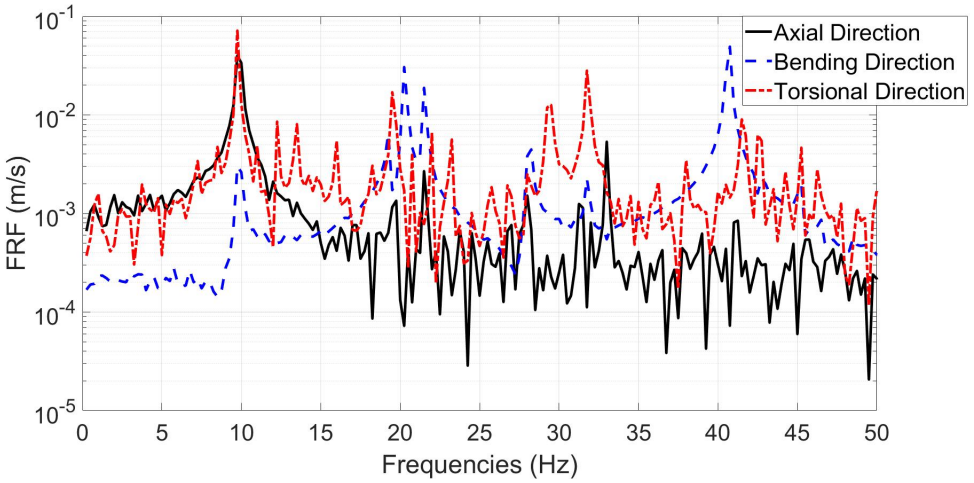

Figure 2.17. Frequency Response Plot of Specimen 2 When It is Stretched by 20 cm and Excited along Axial, Bending and Torsional Directions, Respectively.

2.5. Cross Section Optimization for Phononic Band Gap Maximization

After the creation of inertial amplification model, the analyses and experimental results are examined, and solid elements are used in optimization process due to their high accuracy. Then, the parameters of the cross section are defined as variables. However, axial stiffness of the structure has to be low to create rotational motion. Otherwise, rotational motion cannot be obtained at low frequencies and amplification of inertia cannot be achieved. The cross section of the structure is defined as both rectangular and trapezoidal. During the optimization process, Global Optimization Toolbox of MATLAB software is used, and genetic algorithm is selected as the optimization method. Analyses are repeated for different population sizes to check the convergence. To minimize the frequency ratio, different optimization studies are conducted by taking pitch (p), number of active coils (n) and outer radius (r) as constants. Gravity (g) is selected its maximum value without causing static or fatigue failure. The cross sectional area is taken as constant during the optimization. In Figure 2.19, the results of the optimization are given.

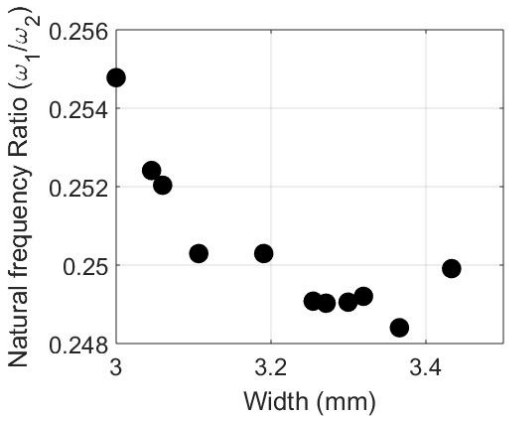

(a)

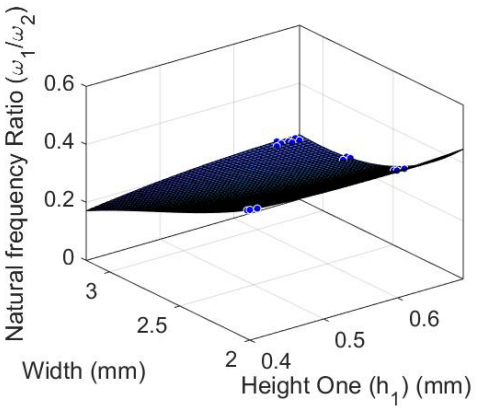

(b)

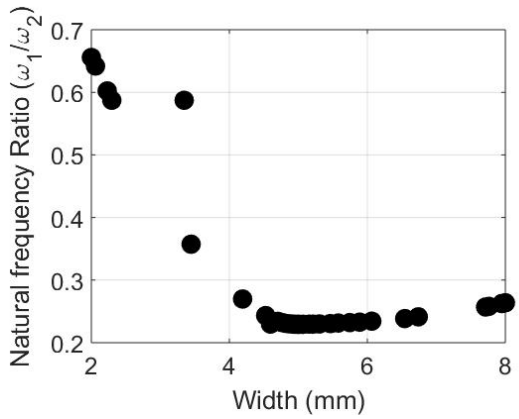

(c)

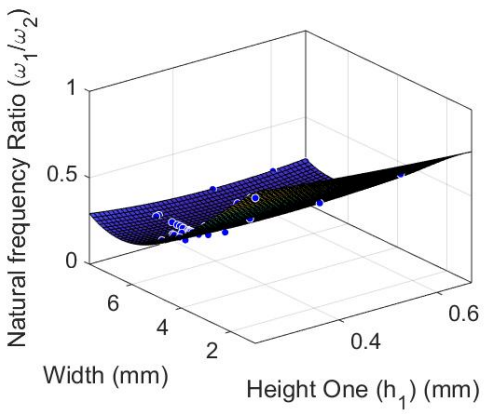

(d)

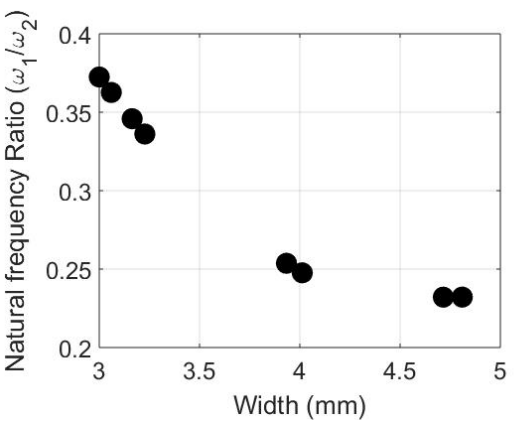

(e)

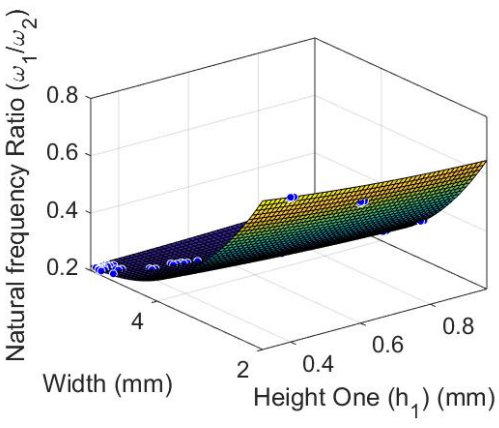

(f)

Figure 2.19. Optimization for Different Cross-Sections and Areas, (a) Rectangular with 6 mm^2 (min=0.248), (b) Trapezoidal with 6 mm^2 (min=0.222), (c) Rectangular with 10 mm^2 (min=0.229), (d) Trapezoidal with 10 mm^2 (min=0.215), (e) Rectangular with 12 mm^2 (min=0.232), (f) Trapezoidal with 10 mm^2 (min=0.216).

In Figure 2.19, pitch (p =23 mm), number of active Coils (n =3), cross sectional area (A), gravity (g =196 m/s^2) and outer radius (r =15 mm) are taken as constant. Results show that minimum frequency ratios are achieved at trapezoidal cross sections but the stress level of these sections are higher than the rectangular ones. The optimum result is obtained when the cross sectional area is 10 mm^2, and minimum frequency ratio (ω_1/ω_2) is about 0.215 when b_1 =0.38 mm, h =5.8 mm, p =2.3 mm, d =3.0 mm and g =196 m/s^2. The outer diameter of the disk is 3.2 mm and their thickness is 5 mm. The first natural frequency is equal to 49.2 Hz with axial-torsional mode shape and the second natural frequency is equal to 229.1 Hz with bending mode shape.

The finite element model of the double helical spring (see Figure 2.20) is created to see the mode shapes and natural frequencies. The system is excited from the bottom surface and top surface only allowed to translate and rotate in the y direction as in the inertial amplification model. The steel is used as a material both in springs and disks. The first natural frequency is obtained at 58.0 Hz, which slightly different from the inertial amplification model (49.2 Hz). The second natural frequency is 233.6 Hz which is very similar (229.1 Hz). The differences between optimization results and finite element model are originated from the mass and stiffness change of the disks. The transmissiblity plot can be seen in Figure 2.21. Transmissibility is less than 1 between 86 Hz to 233 Hz which is quite large isolation bandwidth.

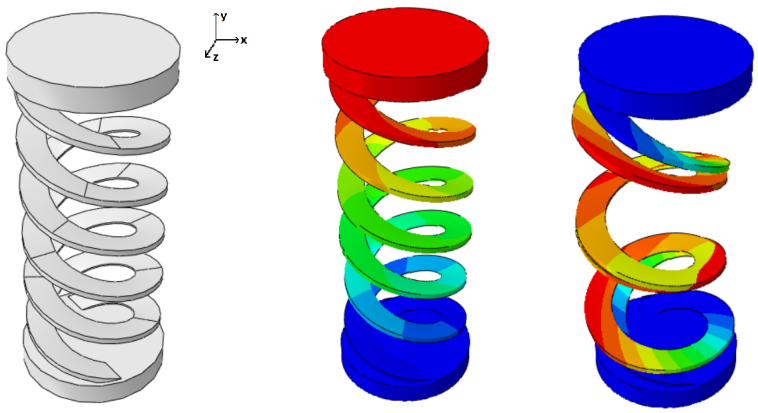

(a) (b) (c)

Figure 2.20. (a) CAD Model of Double Helical Spring in which the Cylindrical Surface of the Upper Disks has Roller Boundary Condition and the Bottom Disk is Fixed, (b) First Natural Frequency (58.0 Hz), (c) Second Natural Frequency (233.6 Hz).

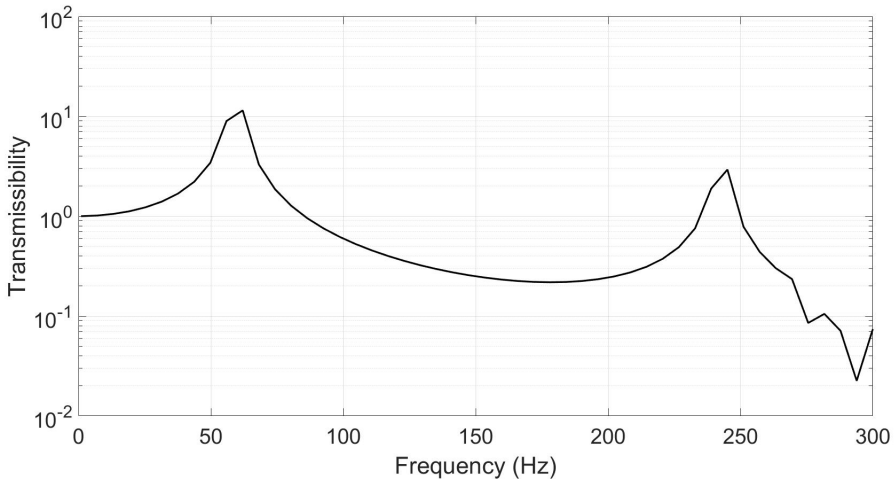

Figure 2.21. Transmissibility Plot of Optimized Double Spring Mechanism.

To realize the boundary condition of the upper disk, three straight wires are attached to the periphery of the disk with equal spacing (120°) and their free ends are fixed to increase the bending stiffness (see Figure 2.22). The length of the wires are taken as 50 mm and their diameters are 1 mm. For this system, the frequency ratio of the mechanism becomes 0.5. Hence, it is much larger than the optimization result (0.215). The length and diameter of the wires are changed but no significant improvement occurred to obtain wide band gaps.

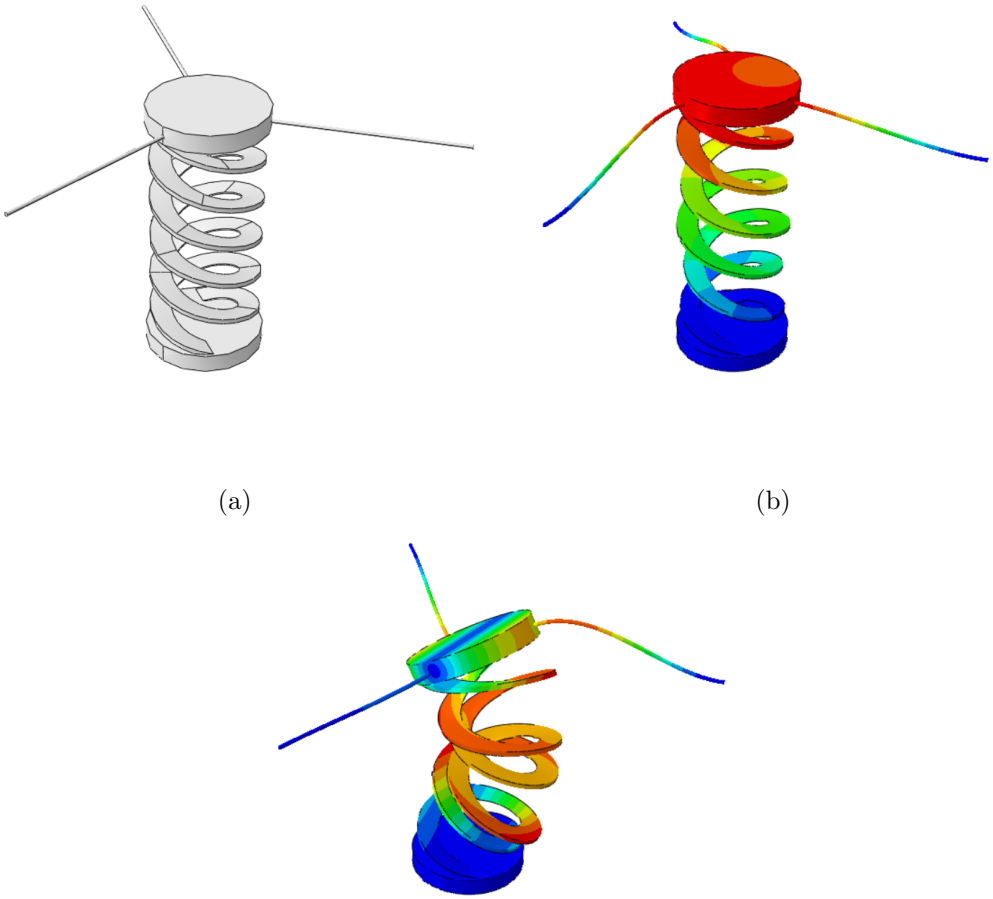

(a) (b)

(c)

Figure 2.22. (a) CAD Model of Double Helical Spring with Attached Wires, (b) First Natural Frequency (104.8 Hz), (c) Second Natural Frequency (210.3 Hz).

3. PROPOSED MECHANISM

The analyses conducted at Chapter 2 show that LADD model has low bending stiffness. For this reason, wide band gaps cannot be obtained by the optimization of the design variables at low frequencies. A major design change is required to increase the bending stiffness of the structure. Therefore, a unit cell mechanism with two rings is proposed (see Figure 3.1(a)). When an array is created with the proposed unit cells, the rings with mass m are constrained to translate axially. However, the rings with mass m_a can translate axially and also rotate. Bending stiffness of the array will be much higher and wider band gaps than LADD mechanism can be obtained due to these constraints.

An analytical model is constructed based on lumped elements (see Figure 3.1(a)) to calculate the band depth (attenuation) of the mechanism. In Figure 3.1(a), the upper ring with mass m only translates with displacement x_{i+1} when the base moves axially by assuming $\beta_i = 0$. Moreover, the lower ring with mass m_a has both translational displacement (x_{i+1}) and angular displacement (β_{i+1}). Therefore, an axial input to the unit cell (x_i) generates axial (x_{i+1}) and rotary (β_{i+1}) motion.

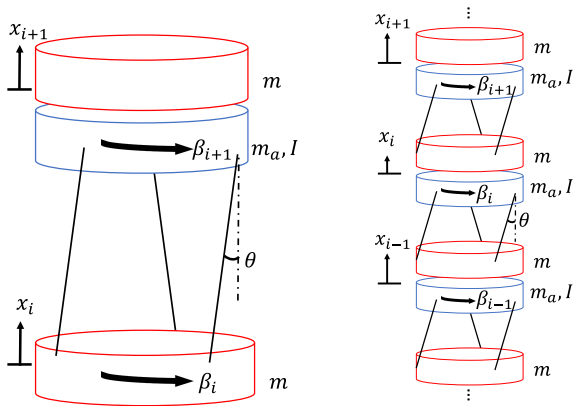

(a) (b)

Figure 3.1. The Proposed Mechanism, (a) Unit Cell, (b) A 1D Array of the Unit Cell.

The wires are modelled as straight beams to calculate the transmissibility and the phononic band structure. Assumption is made due to their high pitch angles, and deflection and boundary conditions of the beam (see Figure 3.2) are modelled to calculate the stiffness.

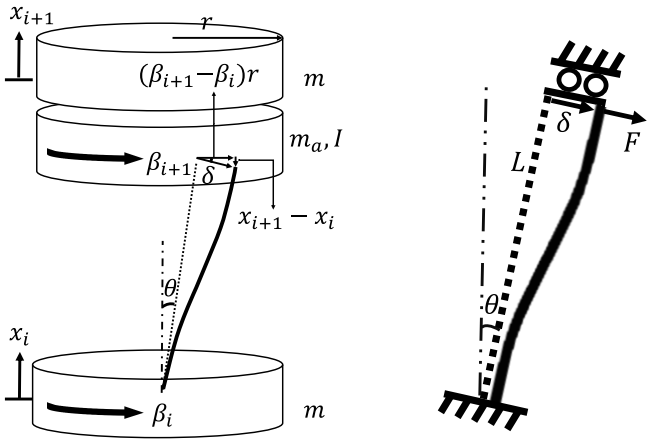

(a) (b)

Figure 3.2. Deflection and the Simplified Boundary Conditions of the Wires, (a) Deflection, (b) Simplified Boundary Conditions.

Considering small deflections, the stiffness of the wires [63, 64] can be calculated as (see Figure 3.2(b))

$$\frac{F}{\delta} = k_w = \frac{12EI_{wire}}{L^3} \tag{3.1}$$

As a result of the geometry (Figure 3.2(a)), relationship between angular and axial displacements can be expressed as

$$\beta_{i+1} - \beta_i = \frac{(x_i - x_{i+1})}{r\tan\theta} \tag{3.2}$$

With the help of Equation 3.2, it can be seen that the angular and axial motions of the disk with mass m_a are coupled. Therefore, in the unit cell mechanism, both rotational and translational motion (Figure 3.2(a)) is obtained when the wires are deflected. Potential energy of the unit cell can be calculated from the deflection (δ),

which can be found as

$$\delta = \frac{r(\beta_{i+1} - \beta_i)}{\cos\theta} = \frac{(x_i - x_{i+1})}{\sin\theta} \tag{3.3}$$

When 3 wires are connecting the disks with mass m and m_a, and assuming that x_i as input displacement ($\beta_i = \dot{\beta}_i = 0$), potential and kinetic energy of the unit cell becomes

$$V = \frac{1}{2}(3k_w)(\delta)^2 = \frac{1}{2}(3k_w)\frac{(x_i - x_{i+1})^2}{\sin^2\theta} \tag{3.4}$$

$$T = \frac{1}{2}(m + m_a)\dot{x}_{i+1}^2 + \frac{1}{2}I\dot{\beta}_{i+1}^2 \tag{3.5}$$

When Equation 3.2 is used in Equation 3.5, T becomes

$$T = \frac{1}{2}(m + m_a)\dot{x}_{i+1}^2 + \frac{1}{2}I\frac{(\dot{x}_i - \dot{x}_{i+1})^2}{r^2\tan^2\theta} \tag{3.6}$$

Potential energy equation (Equation 3.4) shows that effective axial stiffness of the structure is equal to

$$k_{eff} = \frac{3(k_w)}{\sin^2\theta} \tag{3.7}$$

Reference [67], which include finite element models for helical flexures, are compared during the calculation of the effective axial stiffness of the mechanism for verification of the analytical model. The difference between the models is around 10-15 percent for stiffness. The Lagrange method [55] is used with verified analytical model considering x_i as input and x_{i+1} as output displacement, and equation of motion of the unit cell can be found as

$$\left(m + m_a + \frac{I\cot^2\theta}{r^2}\right)\ddot{x}_{i+1} + k_{eff}x_{i+1} = \left(\frac{I\cot^2\theta}{r^2}\right)\ddot{x}_i + k_{eff}x_i \tag{3.8}$$

The effective mass of the unit cell can be seen as the term that multiplies $\ddot{x}_{i+1}$. Effective mass of the unit cell becomes much larger than $m + m_a$ when the angle θ is small because of the inertial amplification. Besides, the first resonance and antiresonance frequencies are calculated as

$$\omega_{p1} = \sqrt{\frac{k_{eff} r^2}{(m + m_a) r^2 + I \cot^2 \theta}} \tag{3.9}$$

$$\omega_{z1} = \sqrt{\frac{k_{eff} r^2}{I \cot^2 \theta}} \tag{3.10}$$

Finally, transmissibility of the structure becomes

$$TR(\omega) = \left| \frac{1 - \left(\frac{\omega}{\omega_{z1}}\right)^2}{1 - \left(\frac{\omega}{\omega_{p1}}\right)^2} \right| \tag{3.11}$$

At large frequencies ($\omega >> \omega_{z1}$), transmissibility equation can be simplified as

$$TR_\infty = \left(\frac{\omega_{p1}}{\omega_{z1}}\right)^2 = \frac{I \cot^2 \theta}{(m + m_a) r^2 + I \cot^2 \theta} \tag{3.12}$$

Equation 3.12 shows that TR_∞ is independent of the stiffness k_{eff}. However, the effect of higher natural frequencies are neglected in the analytical model because it is SDOF. For isolation band depth calculation, Equation 3.12 is still useful.

To attain the phononic band structure of the 1D array (see Figure 3.1(b)), equation of motion for x_i and its neighbors is expressed by the Lagrange method. The phononic band structure is found by Bloch's theorem.

$$\left(m + m_a + \tfrac{2I \cot^2 \theta}{r^2}\right) \ddot{x}_i - \left(\tfrac{I \cot^2 \theta}{r^2}\right) \ddot{x}_{i-1} - \left(\tfrac{I \cot^2 \theta}{r^2}\right) \ddot{x}_{i+1} + k_{eff} \left(2x_i - x_{i-1} - x_{i+1}\right) = 0 \tag{3.13}$$

$$x_{i-1} = x_i e^{-i\gamma} \tag{3.14}$$

$$x_{i+1} = x_i e^{i\gamma} \tag{3.15}$$

where γ represents the wave number. Angular displacement does not appear in Equation 3.13 because they are written in terms of axial displacements (see Equation 3.2). Equation 3.13, Equation 3.14, and Equation 3.15 can be solved together to attain the phononic band structure. Thus, the dispersion relation is found as

$$\cos(\gamma) = 1 - \frac{(m + m_a)\omega^2 r^2}{2(r^2 k_{eff} - \omega^2 I \cot^2\theta)} \tag{3.16}$$

The phononic band structure diagrams are examined in Section 3.2.

3.1. Finite Element Models

In the analytical model of the unit cell (Figure 3.1(a)), it is assumed that the ring with mass m has axial motion, and the ring with mass m_a has both axial and rotational motion. For this reason, the rings m and m_a have to stay parallel to each other. Low torsional stiffness and high bending stiffness are achieved thanks to this constraint. For this purpose, cross flexure mechanisms can be considered [68, 69].

3.1.1. Cross Flexure Mechanism

In literature, cross flexure mechanisms are generally used in micro manipulators, precision positioning and optical focusing systems [68–70]. Cross flexure mechanism can be used in the proposed mechanism due to its low torsional and high bending stiffness. A cross flexure mechanism which has two separate rings is designed. Connection of the rings is realized via elastic beams (Figure 3.3(a)). The system allows rotation under small torques thanks to the flexure beams. However, large widths of the structure prevent bending motion in which the two rings tend to separate from each other. An example cross flexure mechanism can be seen in Figure 3.3. The inner diameter of the rings are 100 mm, the overall height ($2h$) is 60 mm and the dimensions of the flexure beams are 80 mm×22 mm×0.2 mm. To allow 4 mm clearance on both sides width of

the flexure beam is taken as 8 mm less than h=30 mm. The flexure beams are made up of steel and the rings are made up of PLA (E=3.5 GPa, ρ=1190 kg/m^3, μ=0.36). Non-linear geometry solver of the ABAQUS software is used for finite element model of the structure. 3D tetrahedral mesh is used during the analysis.

The first and second natural frequencies of the cross flexure mechanism are at 4.3 Hz and 104.0 Hz, respectively. The first mode shape is in the torsional direction (see Figure 3.3(b)), and the second mode shape is in the bending direction (see Figure 3.3(c)). Notice that natural frequency of bending mode is much larger than the frequency of the torsional mode. By changing the width of the flexures and their thickness, the ratio of torsional and bending natural frequencies can be decreased further.

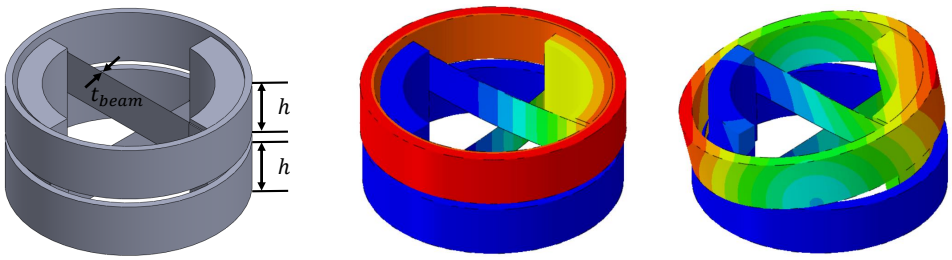

(a) (b) (c)

Figure 3.3. Cross Flexure Mechanism and Its Mode Shapes, (a) CAD Model, (b) First Mode Shape (4.3 Hz), (c) Second Mode Shape (104.0 Hz).

To form a periodic structure the cross flexure mechanisms can be connected in series. Axial motion can be transformed into rotary motion via these connections. However, to achieve the constraint of the upper ring, which translates without rotation (see Figure 3.1(a)), a new mechanism has to be designed and integrated.

3.1.2. Spiral Flexures

In the literature, spiral flexures are generally used to achieve high bending and low axial stiffness [71–75]. They are generally used in compressor motor assembly supports, linear Stirling cryocoolers' displacers and modal shakers. To connect individual unit cells to each other 4 bolts near the center of the spiral flexures are used. Besides, there

should be places for the supports, which are used to connect the rings inside the unit cells. Moreover, connection holes are required to connect the spiral flexures to upper ring, and it should be inside between the inner and outer diameter of the upper ring. Additionally, having high in-plane (radial) stiffness and low out-of-plane (axial) stiffness are the main aim of the spiral structure of the flexures. These constraints can be seen in Figure 3.4(a). Due to constraints of the cross flexure mechanism, lower ring rotates freely, so the clearance for the lower ring should be more than 10 mm. On the contrary, upper ring cannot rotate, so the clearance can be less than 5 mm. However, bending stiffnesses of the structure has to be similar because of the symmetry. For design process, the symmetry of the bending directions should be considered. According to the constraints, the spiral arms are defined by splines and, two types of design are developed. Notice that, in both designs, symmetry constraint is taken into account. Designed steel spiral flexures can be seen in Figure 3.4(b) and Figure 3.4(c).

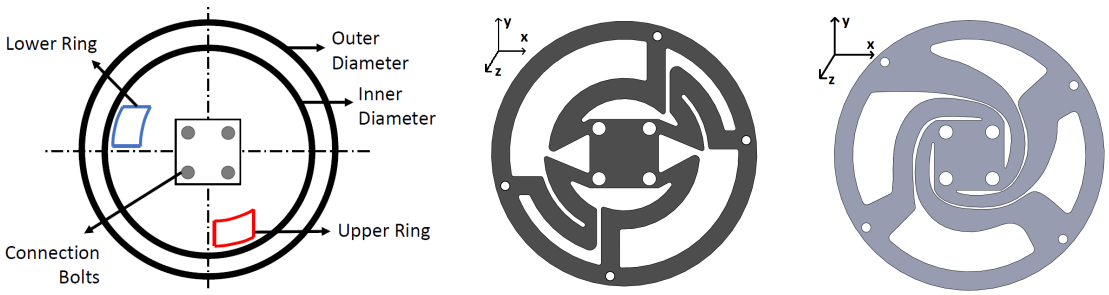

(a) (b) (c)

Figure 3.4. Design Constraints and CAD Models of Spiral Flexures, (a) Design Constraints, (b) First Design, (c) Second Design.

The finite element models of the spiral flexures are constructed, and the first 3 natural frequencies and mode shapes can be seen in Table 3.1 and Figure 3.5. In the analysis, the outer edge of spiral flexure is fixed and outer diameter is 116 mm. Thickness is taken 0.5 mm to avoid wrappage originated from laser cutting.

Table 3.1. The First Three Natural Frequencies of the Spiral Flexures Obtained from FE Analysis.

First Design (Hz)	**Second Design (Hz)**
300.5	302.6
404.9	320.3
549.5	349.8

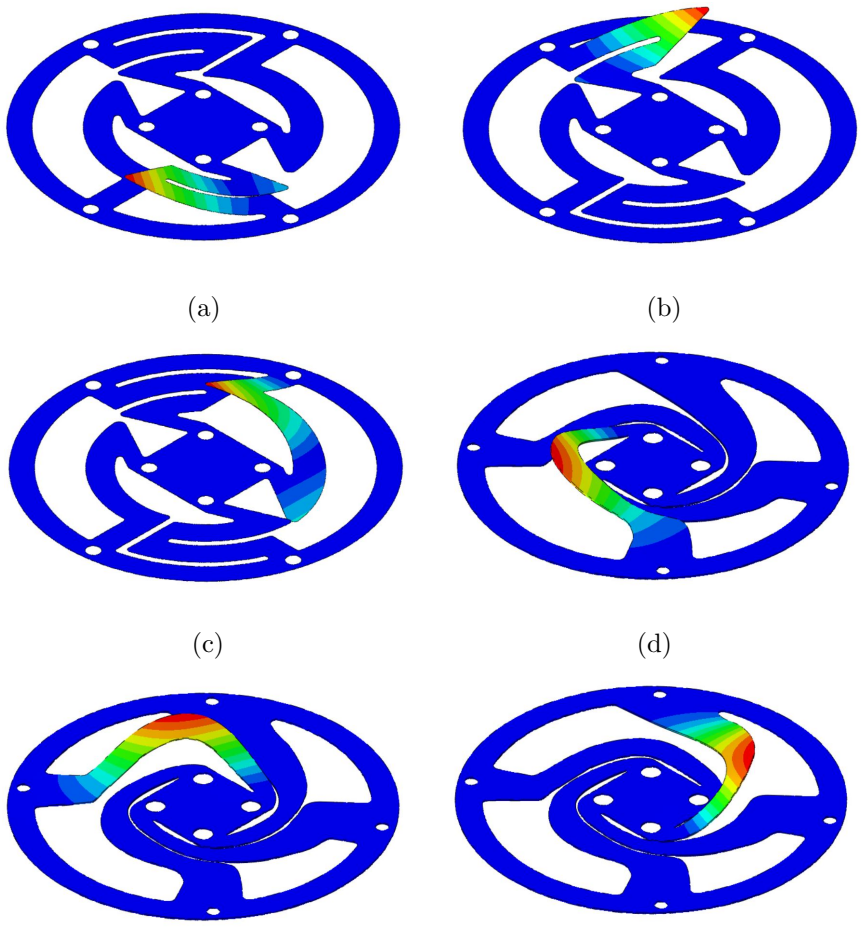

(a) (b) (c) (d) (e) (f)

Figure 3.5. The First 3 Mode Shapes of the First Design, (a) First Mode Shape (300.5 Hz), (b) Second Mode Shape (404.9 Hz), (c) Third Mode Shape (549.5 Hz), and First 3 Mode Shapes of the Second Design (d) First Mode Shape (302.6 Hz), (e) Second Mode Shape (320.3 Hz), (f) Third Mode Shape (349.8 Hz).

Table 3.2. The Stiffnesses of the Spiral Flexures Obtained from FE Analysis.

	k_x **(N/m)**	k_y **(N/m)**	k_z **(N/m)**	k_x/k_z	k_y/k_z
First Design	880.0	1159.0	25.7	34.2	45.1
Second Design	1130.0	1240.0	1.4	807.1	885.7

According to the results, first design has higher natural frequencies, and both designs are out of target isolation frequency. Stiffness values of the first design and second design are listed in Table 3.2, and it shows that in second design bending stiffness is higher and axial stiffness is much lower than the first one. Therefore, second design is selected due to its high bending over axial stiffness ratios. Further analysis is required because the mass of the unit cells affects the natural frequencies of the spiral flexures. To see the dynamic characteristics, 4 cylinders having a total mass 0.5 kg are added to the central bolt holes. The first two mode shapes are calculated (Figure 3.6(a) and Figure 3.6(b)). The first mode shape is in the axial direction (10.8 Hz), and the second mode shape is in the bending direction (19.4 Hz). Results show that the second natural frequency is not far from the first one.

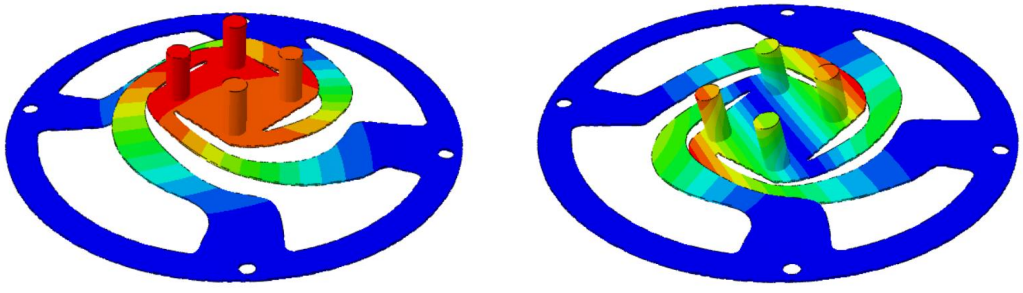

(a) (b)

Figure 3.6. Mode Shapes of the Spiral Flexure with 0.5 kg Additional Mass (a) First Mode Shape (10.8 Hz), (b) Second Mode Shape (19.4 Hz).

Two parallel spiral flexures with a spacing of 30 mm are used (Figure 3.7) to increase the bending to axial natural frequency ratio. By using two parallel spiral flexures, the mass and axial stiffness of the system are doubled. Therefore, the first

natural frequency (11.2 Hz) is very close the single spiral flexure case (10.8 Hz), but bending mode of the parallel flexures (185.2 Hz) is much higher than the single flexure case (19.4 Hz). For this reason, spiral flexures are integrated into the top and bottom surfaces of the upper ring for each unit cell of the periodic structure.

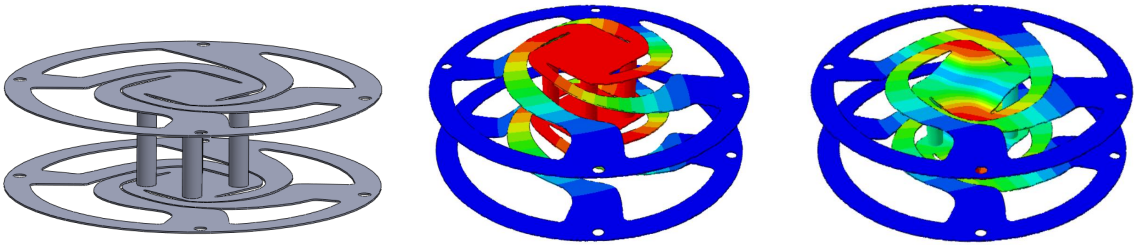

(a) (b) (c)

Figure 3.7. Mode Shapes of the Parallel Spiral Flexure with 1 kg Additional Mass (a) CAD Model, (b) First Mode Shape (11.2 Hz), (c) Second Mode Shape (185.4 Hz).

3.1.3. Helical Wires

In the literature, cylindrical helical structures are generally utilized to convert axial motion into rotational motion [15, 19, 67, 76]. Their frictionless design made these compliant mechanisms ideal for small rotations. An example helical compliant mechanism can be seen in Figure 3.8, in which the disks' thicknesses are 10 mm and their diameters are 100 mm. Three 100 mm long wires with 2 mm radii are placed at 120 degrees around the disks for symmetry. 60 degree is selected as the helix angle of the wires. Steel is used for the overall structure. By fixing the bottom disk and giving roller boundary condition to the cylindrical surface of the top disk, the first and the second natural frequencies are calculated as 122.2 Hz (Figure 3.8(b)) and 827.4 Hz (Figure 3.8(c)), respectively. As it can be seen from Figure 3.8(b), while the top disk moves towards the bottom one, it also rotates.

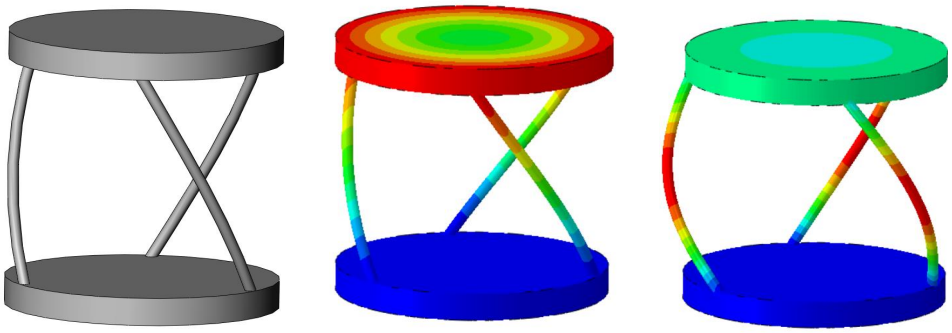

(a) (b) (c)

Figure 3.8. Helical Flexure Hinges, (a) CAD Model, (b) Axial-Torsional Mode Shape (122.2 Hz), (c) Bending Mode Shape (827.4 Hz).

Cross flexure mechanism, parallel spiral flexures and helical wires are integrated in the final design, and a compliant axial to rotary motion conversion mechanism is constructed (Figure 3.9). Briefly, input axial displacement transmitted into the bottom ring of the mechanism (m_a) via helical wires. Rotational movement for the bottom ring is created by the helical wires, but rotation of the upper ring (m) is prevented by parallel spiral flexures, which increase the bending stiffness of the structure. Therefore, the upper ring translates without rotation. Besides, the rings with mass m and m_a remain parallel to each other as m_a rotates with respect to m due to cross flexure constraints. To create a periodic structure, plates and bolts are attached above the upper ring. The proposed lumped parameter unit cell is realized as a compliant axial to rotary motion conversion mechanism (see Figure 3.1(a) and Figure 3.9(c)).

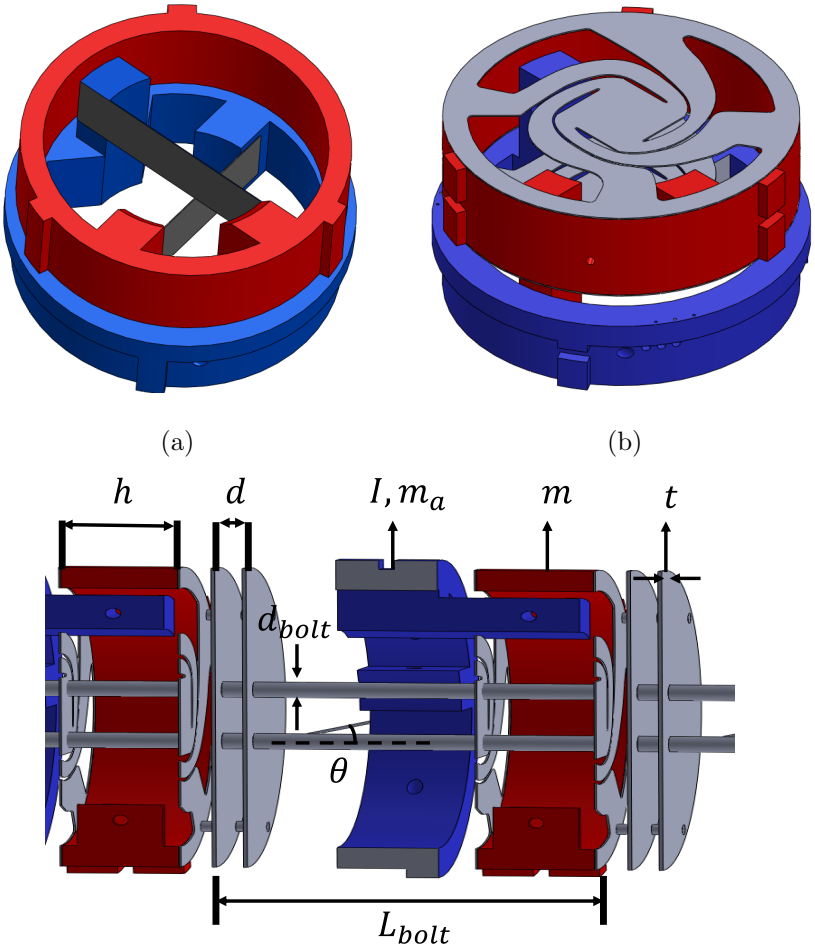

Figure 3.9. Separated Parts of the Unit Cell Mechanism and Integrated Final Design (a) Flexure Beams within Cross Flexure, (b) Parallel Spiral Flexures within Cross Flexure, (c) Unit Cell When Helical Wires, Connection Bolts and Connection Plates are Integrated.

3.2. Parametric Studies for Bandwidth Maximization

Maximum bandwidth is achieved between the first two natural frequencies (w_1 and w_2) of the unit cell mechanism. To maximize the band gap, various parametric studies are conducted. The objective is to minimize w_1/w_2 ratio. However, small finite element mesh is necessary because of complex geometry and connection properties of the structure. As a result, model preparation and solution time is high. Therefore, all design variables are examined separately because changing all the parameters at

the same time is not feasible. At the beginning, geometric parameters of the unit cell are determined based on simplified models. In simplified models (see Figure 3.3 and Figure 3.8), ring height (h) which also affects width of the flexure beams, flexure beams thickness (t_{beam}), and helical wire radii (r_{wire}) are examined. The results can be seen in Tables 3.3, Table 3.4 and Table 3.5.

Height of the rings (Figure 3.3(a)) is examined at the parametric study to determine the size of the rings. The width of the cross flexure beams is 8 mm less than ring height (h) for clearance. The thickness t_{beam} and length of the cross flexures L_{beam} are taken as 0.2 mm and 80 mm, respectively. The inner diameters of the rings are constant and 100 mm. In Table 3.3, torsional stiffness is increased when the height of the ring increases. However, the mass of the structure is increased with increasing the thickness of the rings. According to the parametric study, w_1/w_2 reaches minimum value when h=30 mm.

Table 3.3. Natural Frequencies and Frequency Ratio vs. Ring Height (h).

h (mm)	w_1 (Hz)	w_2 (Hz)	w_1/w_2
20	4.1	91.9	0.045
30	4.3	104.0	0.041
40	4.4	105.0	0.042

Further analyses have been done for cross flexure beam thickness with the selected ring height. In Table 3.4 (L_{beam}=80 mm and w_{beam}=22 mm), when beam thickness is increased, the torsional stiffness is also increased. The smallest w_1/w_2 ratio is obtained at 0.2 mm. However, to create a periodic structure (see Figure 3.9(c)) cross flexure mechanism need to carry steel connection plates. To see how additional mass affects the natural frequencies, an estimated 0.2 kg is added at the top of the cross flexure mechanism. In Table 3.4, results show that frequency ratios of the cross flexure mechanism with additional mass case are the same with the massless ones, but natural frequencies of the mechanism are considerably decreased. w_1/w_2 ratios increase when t_{beam} increases. However, t_{beam}=0.3 is preferred due to laser cut manufacturing

constraints and avoiding wrappage originated from residual stresses.

Table 3.4. Natural Frequencies and Frequency Ratio vs. Flexure Beam Thickness (t_{beam}) with and without Mass.

	Without additional mass			With 0.2 kg mass		
t_{beam} (mm)	w_1 (Hz)	w_2 (Hz)	w_1/w_2	w_1 (Hz)	w_2 (Hz)	w_1/w_2
0.2	4.3	104.0	0.041	2.0	48.7	0.041
0.3	7.3	114.5	0.063	3.5	55.3	0.063
0.4	11.2	105.6	0.106	5.3	50.2	0.106

When the radius of the helical wires are examined, increasing the wire diameter, increases the natural frequencies significantly (see Table 3.5). Minimum frequency ratio is achieved for 0.5 mm radius, but reducing the wire radius less than 0.5 mm does not improve w_1/w_2 ratio much. Besides, for lower values the bending modes of the wires negatively affect the band gap of the unit cell.

Table 3.5. Natural Frequencies and Frequency Ratio vs. Radius of the Helical Wires (r_{wire}).

r_{wire} (mm)	w_1 (Hz)	w_2 (Hz)	w_1/w_2
0.5	5.8	70.6	0.082
1	22.7	260.4	0.087
2	122.2	827.4	0.148

After the parametric studies of the simplified models, the unit cell is constructed with 0.5 mm helical wire radius (r_{wire}), 30 mm ring height (h) and 0.3 mm flexure beam thickness (t_{beam}). Thickness of the connection plate is taken as 1 mm. There are two parallel connection plates which are located 7 mm (d) away from each other above the ring with mass m (see Figure 3.9(c)). Using one plate causes reduction in the bending modes at low frequencies. Integration of two plates for large d increase the

bending modes. Therefore, d which allow proper clearance for vibration, is selected as the highest possible value. Additional parametric studies are conducted for connection bolt length (L_b) and connection bolt diameter (d_{bolt}) with the complete unit cell.

The aim of the parametric studies is the maximization of the isolation bandwidth, which is the minimization of w_1/w_2. Having high level of attenuation within the isolation bandwidth is another goal. According to Equation 3.12, transmissibility (TR_∞) depends on $(m + m_a)$, I, r, and θ. Considering the mass of the connection plates and bolts it is assumed that $m = 2m_a$. When $I = m_a r^2$, Equation 3.12 can be simplified to TR_∞=$\cot^2\theta/(3+\cot^2\theta)$. If the target level of transmissibility is selected as 0.75, θ can be calculated as 18°. The length of the helical wires can be changed by changing helix angle and bolt length. Due to the commercial bolt length constraints, length of the bolt is selected as a variable rather than the helical wires length. Results are given in Table 3.6 and Table 3.7.

For various connection bolt diameters and lengths, the first, second and fourth natural frequencies and their ratios with respect to the first natural frequency are given in Table 3.6 and Table 3.7. When the frequency response functions of the unit cell are considered, the second and the third natural frequencies do not affect the transmissibility because of their non-axial effects, but increasing the second natural frequency can increase the fourth one. Therefore, both w_1/w_2 and w_1/w_4 are considered.

In Table 3.6 (L_{bolt}=90 mm and θ=18°), when connection bolt diameter is increased, the first natural frequency slightly increases since the head and nut parameters are changed. Increasing bolt diameter increases the bending natural frequency. The fourth natural frequency is axial-torsional coupling mode, and it is increased when bolt diameter is increased. However, transmissibility is affected by the minimum w_1/w_4 ratio, which achieved for 6 mm bolt diameter.

Table 3.6. Natural Frequencies and Frequency Ratio vs. Connection Bolt Thickness (d_{bolt}).

d_{bolt} (mm)	w_1 (Hz)	w_2 (Hz)	w_4 (Hz)	w_1/w_2	w_1/w_4
4	12.7	53.0	58.2	0.240	0.218
6	12.9	58.4	82.6	0.221	0.156
8	13.3	64.1	83.9	0.207	0.159

A final parametric study is conducted to determine the length of the connection bolts (L_b), which determines the helical wires' length and the bending natural frequencies. The results can be seen in Table 3.7. Increasing the bolt length decreases all natural frequencies and the frequency ratios. If a 1D array with multiple unit cells is examined, its bending modes govern the upper limit of the stop band. The bending modes will arise at low frequencies for large L_b values. Thus, L_b =90 mm is chosen. Here, d_{bolt}=6 mm and θ=18°.

Table 3.7. Natural Frequencies and Frequency Ratio vs. Length of the Bolts.

L_b (mm)	w_1 (Hz)	w_2 (Hz)	w_4 (Hz)	w_1/w_2	w_1/w_4
80	15.8	64.9	83.8	0.243	0.189
90	12.9	58.4	82.6	0.221	0.156
100	11.7	55.1	81.7	0.212	0.143

By considering the manufacturability of the design, two different materials are used within the unit cell. PLA is used for the rings. Steel is used for flexures, plates, wires, nuts and bolts. Helical wire radii and cross flexure mechanism inner diameter are taken as 0.5 mm and 100 mm, respectively. Ring heights are 30 mm, and flexure beam dimensions are 90 mm×22 mm×0.3 mm. Helix angle of the wires are 72 degree ($\theta = 18°$), and their lengths are 80 mm. The helical wires are integrated around the periphery of the rings with 61 mm radius (r). $m + m_a$ and I can be calculated as 0.73 kg and 8.56×10^{-4} kg.m^2, respectively. Using Equation 3.7, the effective axial stiffness

of the structure can be found as $(3k_w/\sin^2\theta)$. However, two parallel spiral flexures are utilized (see Figure 3.9(c)), and their axial stiffness $2k_s$ can be found as 2×1.37 N/mm. Additionally, torsional stiffness of the cross flexure beams can be calculated as

$$2k_{tcross} = \frac{2EI_{beam}}{L_{beam}} \tag{3.17}$$

Cross flexure beams are attached to rings with outer radius r. Also, helical wires are at the outer radius of the rings to convert axial motion into rotary one as depicted in Figure 3.2 and Equation 3.3. Thus, axial stiffness of the cross flexures can be obtained as

$$k_{cross} = \frac{k_{tcross}}{r^2 \tan\theta} \tag{3.18}$$

Consequently, in the unit cell (see Figure 3.9(c)), effective axial stiffness is

$$k_{axial} = \frac{3k_w}{\sin^2\theta} + 2k_s + 2k_{cross} \tag{3.19}$$

For the given parameter values, it can be found as 10.7 N/mm.

When k_{eff} (see Equation 3.9 and Equation 3.10) is replaced by k_{axial} in Equation 3.19, w_{p1} and w_{z1} are found as 9.7 Hz and 11.2 Hz, respectively. Since, w_{p1}/w_{z1} ratio is equal to 0.87, then TR_∞=0.75. It is the target transmissibility level in the isolation bandwidth (see Figure 3.10). In the FE model, w_{p1} and w_{z1} are found as 12.9 Hz and 14.6 Hz, respectively. Despite there is a shift with respect to the analytical frequency values, w_{p1}/w_{z1} ratio is 0.88, which is almost the same with FE study. Furthermore, the FE transmissibility result shows that there is a upper limit for the isolation bandwidth because of the higher frequency modes of the mechanism. These modes are not captured in the SDOF analytical model and transmissibility increases in the FE model as the frequency increases towards the upper limit. Still, transmissibility is lower than 0.75 until $w = 2w_{z1}$ in the FE model.

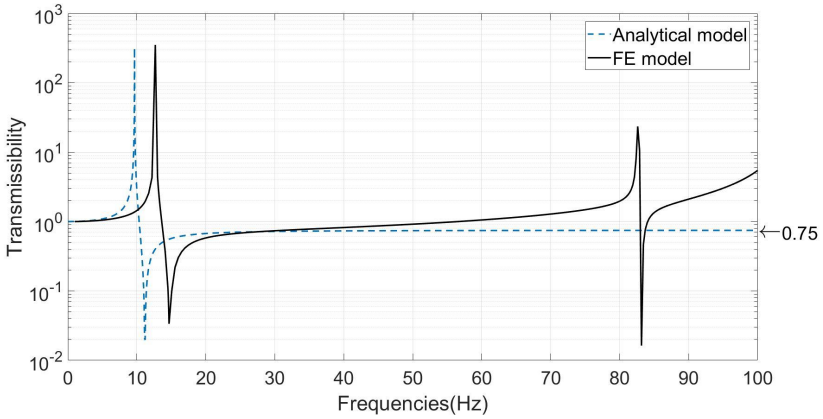

Figure 3.10. Transmissibility Plots of Analytical and FEA Models for the Unit Cell Mechanism.

By solving Equation 3.16 for various helix angles phononic band structure of the designed system can be found (see Figure 3.11). It can be said that the band gap starting frequency can be reduced by decreasing the angle θ because of amplified inertia effect (see the multiplier of $\ddot{x}_i$ term in Equation 3.13). The band gap starting frequency is at 11 Hz for $\theta = 18°$. Furthermore, in the imaginary part of plot, a notch can be seen because of the inertial coupling effect. The frequency of the notch is decreased when θ is decreased. For very small θ values, attenuation above the notch frequency is small. To have significant attenuation at low frequencies, θ is selected as 18°.

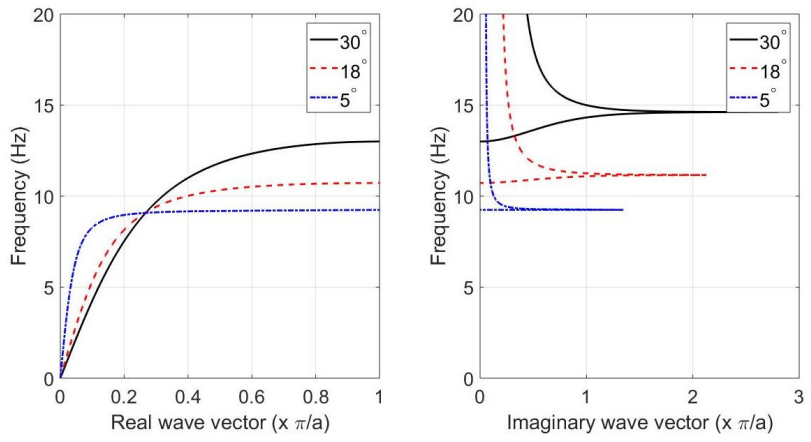

Figure 3.11. Phononic Band Structure with respect to Angle (θ) for the SDOF Unit Cell Mechanism.

Mode shapes and natural frequencies of the unit cell are depicted in Table 3.8. The first, second and fourth mode shapes can be seen in Figure 3.12.

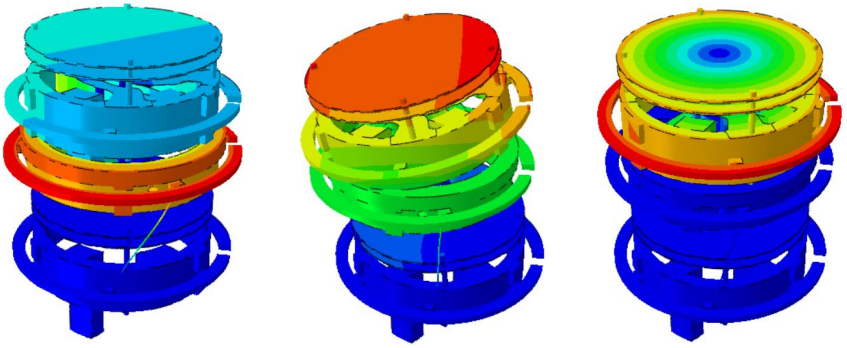

(a) (b) (c)

Figure 3.12. Mode Shapes of the Unit Cell Mechanism, (a) First Mode Shape (12.9 Hz), (b) Second Mode Shape (58.4 Hz), (c) Fourth Mode Shape (82.6 Hz).

Table 3.8. Natural Frequencies and Mode Shapes of the Unit Cell Mechanism. In the Last Row, Mode Shapes have been Represented as Coupled Axial-Torsional (AT) or Bending (B).

Mode Number	1	2	3	4	5	6	7	8	9	10
Frequency (Hz)	12.9	58.4	59.3	82.6	109.6	122.0	150.0	255.9	266.1	293.7
Mode Type	AT	B	B	AT	AT	B	B	B	B	B

Table 3.9 shows mode shapes and natural frequencies of the periodic structure. The first, sixth, seventh and eighth mode shapes are depicted in Figure 3.13.

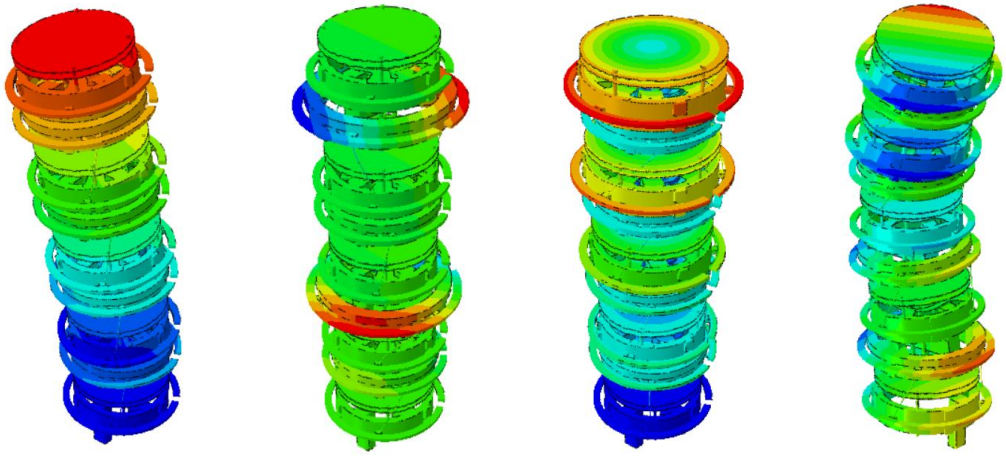

(a) (b) (c) (d)

Figure 3.13. Mode Shapes of the 1D Array with 4 Unit Cells, (a) First Mode Shape (5.6 Hz), (b) Sixth Mode Shape (10.7 Hz), (c) Seventh Mode Shape (25.5 Hz), (d) Eighth Mode Shape (39.2 Hz).

Table 3.9. Natural Frequencies and Mode Shapes of the 1D Array with 4 Unit Cells. In the Last Row, Mode Shapes have been Represented as Coupled Axial-Torsional (AT) or Bending (B).

Mode Number	1	2	3	4	5	6	7	8	9	10
Frequency (Hz)	5.6	5.7	6.2	8.5	10.1	10.7	25.5	39.2	41.0	41.8
Mode Type	B	B	AT	AT	AT	AT	AT	B	B	B

3.3. Experimental Validation

According to the parametric study results, unit cell mechanism (see Figure 3.9(c)) is used to create a 1D array with 4 unit cells, which can be seen in Figure 3.14(a)-3.14(b). Laser cutting method is used for manufacturing of parallel spiral springs and connection plates, and 3D printing method is used for manufacturing unit cell rings. For the connection of the unit cell and the plates, M4 60 mm bolts and M6 90 mm

connection bolts are selected. Snap rings are used for connection of the helical wires and the PLA rings. Additionally, to reduce contact area and provide a unyielding boundary condition, M3 slot head screws are integrated into the PLA rings, and the wires fit inside the slots (Figure 3.14(c)).

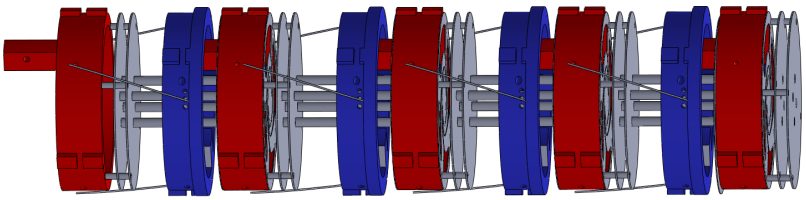

(a)

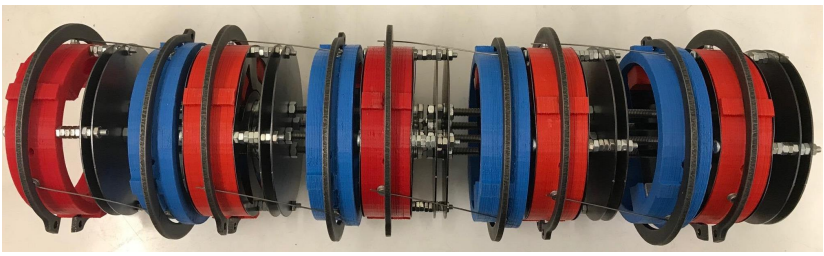

(b)

(c)

Figure 3.14. CAD Model, Prototype and Wire Boundary Condition of the Periodic Structure, (a) CAD Model, (b) Prototype, (c) Zoomed view of Boundary Condition.

During the experiments, the unit cell and periodic structure are tested. Rubber cords are used to hung the structures, and they excited from one end via modal shaker (see Figure 3.15(a) and Figure 3.15(b)). The input and output accelerations are measured by an impedance head and accelerometer, respectively. To decrease the noise effect, the average of 60 measurements are taken.

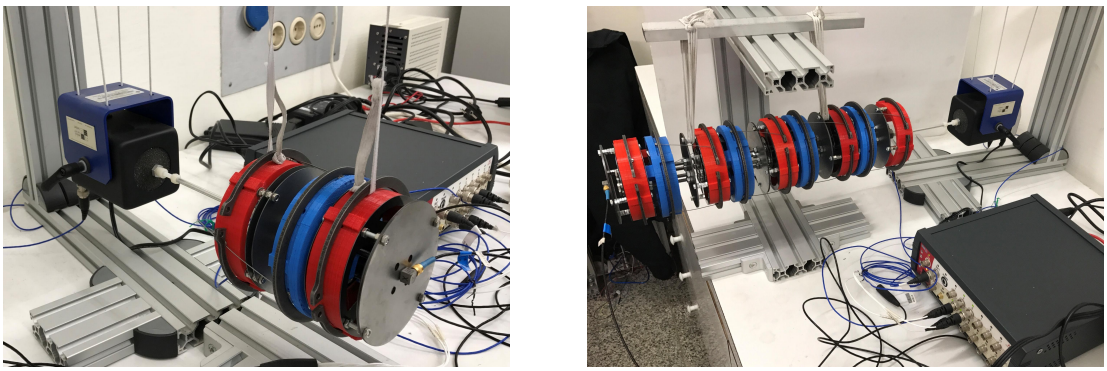

(a) (b)

Figure 3.15. Experimental Setup of the (a) Unit Cell, (b) 1D Periodic Structure Consist of 4 Unit Cells.

Figure 3.16 shows transmissibility of the unit cell. Results of the experiments reveal that transmissibility is less than one between 14 Hz to 48 Hz. Stop band limit ratio is calculated as 3.4, which is quite large. Besides, experimental and FEA resonance frequencies are almost the same. The second and third mode shapes, which can be seen in Figure 3.12 and Table 3.8, are not seen in the transmissibility diagram because an axial input couldn't excite the bending modes. In general, experimental and computational results have a very good correlation.

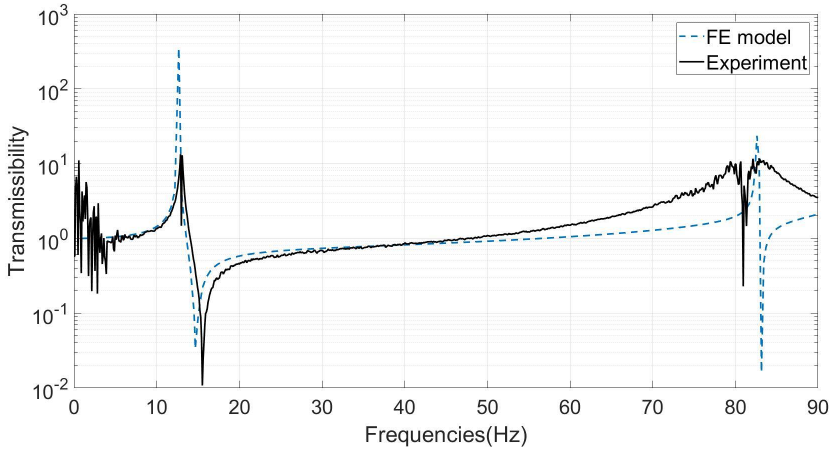

Figure 3.16. Transmissibility Plot of the Unit Cell.

Figure 3.17 shows transmissibility of the periodic structure. Transmissibility is lower than one between 11 Hz to 39 Hz in the experiment results. Stop band limit ratio

is 3.5, which is quite large. Table 3.9 presents that the stop band is obtained between the sixth and eight modes (see Figure 3.13). When the bottom of the structure is excited and the output is measured at the center of the top surface, the seventh mode does not seem as a resonance peak. The reason for this is that displacement at the top center point (see Figure 3.13(c)) is zero, and it appears as an antiresonance notch at 25 Hz (see Figure 3.16). The eighth mode, which is of bending type, governs the upper limit of the stop band. With the maximization of the bending stiffness, a wide and deep stop band is generated. Similarly, experimental and finite element results have a good correlation. Bolt, snap ring prestresses and assembly errors are the reason for the small differences.

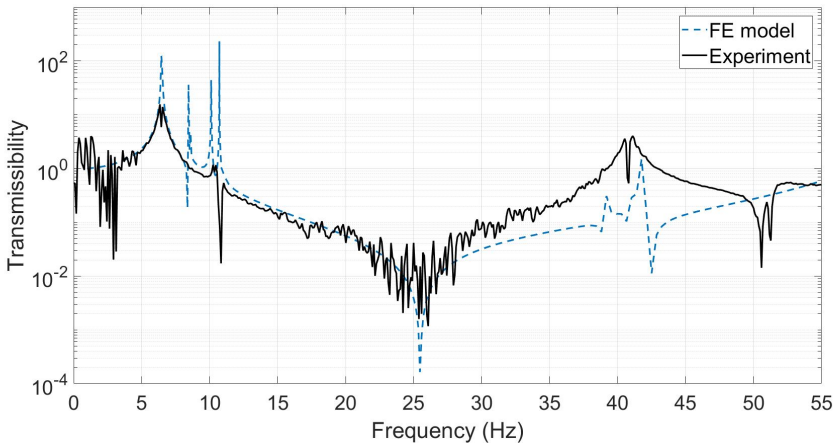

Figure 3.17. Transmissibility Plot of the Periodic Structure with 4 Unit Cells.

4. CONCLUSION

Compliant axial to rotary motion conversion mechanisms are investigated to create phononic band gaps. To obtain stop bands at low frequencies, LADD mechanism is analysed, and its the effective inertia is aimed to be increased. Besides, to maximize the stop band, helical wire theory is examined. Analytical and finite element models of the mechanism are created and validated with experiments. Then, tensile prestress is used and cross sections of helical wires are optimized to achieve wide band gaps. The minimum first two frequency ratio (ω_1/ω_2) is obtained 0.215, which is quite large to acquire wide isolation band gaps. However, in this model idealized roller boundary conditions are used on the cylindrical surfaces of the disks within the system. Realizing this type of boundary condition in a compliant system which prevents backlash and friction problems, is a hard task. To that end, 3 wires per disk are utilized which are in the same plane. Then, the frequency ratio increased to 0.5, which is not sufficient to obtain wide isolation band gap. Helical spring design parameters are changed but still bending natural frequencies of the mechanism cannot be increased. For this reason, a novel axial to rotary motion conversion mechanism is proposed. In the proposed mechanism, stop band of the unit cell is governed by two different types of modes. The lower and the upper limits of the stop band are due to the coupled axial-torsional and bending modes, respectively. Due to their high bending stiffness and low stiffness in axial-torsional motions, cross flexures and spiral flexures are utilized to widen the phononic band gap. Additionally, helical wires are integrated with large helix angles to convert axial motion to rotary one. Analytical and finite element models are used to examine the phononic band structure and the dynamic response attributes. Parametric studies are conducted for bandwidth maximization. Prototypes of the both unit cell and periodic structure is manufactured via 3D printing and laser cutting. In the end, analytical, computational and experimental frequency response results are compared for validation. Consequently, a very wide phononic band gap is achieved at low frequencies with ω_1/ω_2=0.221 and wave propagation through the medium is eliminated in certain range of frequencies where the phononic band gap occurs. Therefore, the mechanism can be used as a vibration isolator or frequency filter.

REFERENCES

1. Ugural, A., *Mechanical design: An integrated approach*, McGraw-Hill Science/Engineering/Math, 2003.

2. Vallance, A. and V. L. Doughtie, *Design of machine members*, McGraw-Hill, 1943.

3. Shigley, J. E. and C. R. Mischke, *Standard handbook of machine design*, McGraw-Hill, 1986.

4. Söylemez, E., *Mekanizma tekniği*, Prestij ajans matbaacılık, 2000.

5. Howell, L. L., *Compliant mechanisms*, John Wiley & Sons, 2001.

6. Söylemez, E., *Mechanisms*, Middle East Technical University, 1979.

7. Söylemez, E., "Classical transmission-angle problem for slider–crank mechanisms", *Mechanism and machine theory*, Vol. 37, No. 4, pp. 419–425, 2002.

8. Berton, S. and J. E. Bolander, "Amplification system for supplemental damping devices in seismic applications", *Journal of Structural Engineering*, Vol. 131, No. 6, pp. 979–983, 2005.

9. Smith, M. C., "Synthesis of mechanical networks: the inerter", *IEEE Transactions on Automatic Control*, Vol. 47, No. 10, pp. 1648–1662, 2002.

10. Smith, M. C. and F.-C. Wang, "Performance benefits in passive vehicle suspensions employing inerters", *Vehicle System Dynamics*, Vol. 42, No. 4, pp. 235–257, 2004.

11. Brzeski, P., T. Kapitaniak and P. Perlikowski, "Novel type of tuned mass damper with inerter which enables changes of inertance", *Journal of Sound and Vibration*, Vol. 349, pp. 56–66, 2015.

12. Lin, M., B. Ravani and S. Velinsky, "Kinematics of the ball screw mechanism", *Journal of mechanical design*, Vol. 116, No. 3, pp. 849–855, 1994.

13. Lin, M., S. Velinsky and B. Ravani, "Design of the ball screw mechanism for optimal efficiency", *Journal of mechanical design*, Vol. 116, No. 3, pp. 856–861, 1994.

14. Palli, G., C. Natale, C. May, C. Melchiorri and T. Wurtz, "Modeling and control of the twisted string actuation system", *IEEE/ASME Transactions on Mechatronics*, Vol. 18, No. 2, pp. 664–673, 2013.

15. Mennitto, G. and M. Buehler, "Ladd transmissions: Design, manufacture, and new compliance models", *Journal of Mechanical Design*, Vol. 119, No. 2, pp. 197–203, 1997.

16. Dong, L., K. Shou, D. R. Frutiger, A. Subramanian, L. Zhang, B. J. Nelson, X. Tao and X. Zhang, "Engineering multiwalled carbon nanotubes inside a transmission electron microscope using nanorobotic manipulation", *IEEE Transactions on Nanotechnology*, Vol. 7, No. 4, pp. 508–517, 2008.

17. Alvo, S., D. Decanini, L. Couraud, A.-M. Haghiri-Gosnet and G. Hwang, "Assembly and mechanical characterizations of polymer microhelical devices", *2014 IEEE/RSJ International Conference on Intelligent Robots and Systems*, pp. 4656–4661, IEEE, 2014.

18. Gaponov, I., D. Popov and J.-H. Ryu, "Twisted string actuation systems: A study of the mathematical model and a comparison of twisted strings", *IEEE/ASME Transactions on Mechatronics*, Vol. 19, No. 4, pp. 1331–1342, 2014.

19. Pottebaum, K. and J. Beaman, "A dynamic model of a concentric LADD actuator", *Journal of dynamic systems, measurement, and control*, Vol. 105, No. 3, pp. 157–164, 1983.

20. Jacobsen, S. C., "Rotary-to-linear and linear-to-rotary motion converters", Feb. 11 1975, US Patent 3,864,983.

21. Hamdi, M., A. Subramanian, L. Dong, A. Ferreira and B. J. Nelson, "Simulation of rotary motion generated by head-to-head carbon nanotube shuttles", *IEEE/ASME Transactions on Mechatronics*, Vol. 18, No. 1, pp. 130–137, 2013.

22. Chen, Z., "Geometric nonlinearity and mechanical anisotropy in strained helical nanoribbons", *Nanoscale*, Vol. 6, No. 16, pp. 9443–9447, 2014.

23. Dai, L., L. Zhang, L. Dong, W. Shen, X. Zhang, Z. Ye and B. Nelson, "Long-range linear elasticity and mechanical instability of self-scrolling binormal nanohelices under a uniaxial load", *Nanoscale*, Vol. 3, No. 10, pp. 4301–4306, 2011.

24. Dong, L., L. Zhang, B. E. Kratochvil, K. Shou and B. J. Nelson, "Dual-chirality helical nanobelts: Linear-to-rotary motion converters for three-dimensional microscopy", *Journal of Microelectromechanical Systems*, Vol. 18, No. 5, pp. 1047–1053, 2009.

25. Xu, D., L. Zhang, L. Dong and B. J. Nelson, "Nanorobotics for NEMS using helical nanostructures", *Encyclopedia of Nanotechnology*, pp. 1715–1721, 2012.

26. Sun, Y., X. Liu, O. Brand, C. Hierold, G. K. Fedder, J. G. Korvink and O. Tabata, *Micro-and nanomanipulation tools*, Vol. 13, John Wiley & Sons, 2015.

27. Dai, L., K.-D. Zhu, W. Shen, X. Huang, L. Zhang and A. Goriely, "Controllable rotational inversion in nanostructures with dual chirality", *Nanoscale*, Vol. 10, No. 14, pp. 6343–6348, 2018.

28. Busool, W. and M. Eisenberger, "Free vibration of helicoidal beams of arbitrary shape and variable cross section", *Journal of vibration and acoustics*, Vol. 124, No. 3, pp. 397–409, 2002.

29. Yildirim, V. and N. İnce, "Natural frequencies of helical springs of arbitrary shape", *Journal of Sound and Vibration*, Vol. 204, No. 2, pp. 311–329, 1997.

30. Yokota, T., T. Taguchi and M. Gen, "A solution method for optimal weight design problem of herical spring using genetic algorithms", *Computers & industrial engineering*, Vol. 33, No. 1, pp. 71–76, 1997.

31. Kessler, D. A. and Y. Rabin, "Stretching instability of helical springs", *Physical review letters*, Vol. 90, No. 2, p. 024301, 2003.

32. Temel, B. and F. Calim, "Forced vibration of cylindrical helical rods subjected to impulsive loads", *Journal of applied mechanics*, Vol. 70, No. 2, pp. 281–291, 2003.

33. Taylor, D. M. and D. P. Hampshire, "Properties of helical springs used to measure the axial strain dependence of the critical current density in superconducting wires", *Superconductor Science and Technology*, Vol. 18, No. 3, p. 356, 2005.

34. Pöllänen, I. and H. Martikka, "Optimal re-design of helical springs using fuzzy design and FEM", *Advances in Engineering Software*, Vol. 41, No. 3, pp. 410–414, 2010.

35. Walters, C., I. Davidson and G. Tuck, "Long sample high sensitivity critical current measurements under strain", *Cryogenics*, Vol. 26, No. 7, pp. 406–412, 1986.

36. Brillouin, L., *Wave propagation in periodic structures: Electric filters and crystal lattices*, Courier Corporation, 2003.

37. Kushwaha, M. S., "Classical band structure of periodic elastic composites", *International Journal of Modern Physics B*, Vol. 10, No. 09, pp. 977–1094, 1996.

38. Yilmaz, C., G. Hulbert and N. Kikuchi, "Phononic band gaps induced by inertial amplification in periodic media", *Physical Review B*, Vol. 76, No. 5, pp. 1–9, 2007.

39. Yilmaz, C. and G. Hulbert, "Theory of phononic gaps induced by inertial ampli-

fication in finite structures", *Physics Letters A*, Vol. 374, No. 34, pp. 3576–3584, 2010.

40. Kushwaha, M., B. Djafari-Rouhani and L. Dobrzynski, "Sound isolation from cubic arrays of air bubbles in water", *Physics Letters A*, Vol. 248, No. 2, pp. 252–256, 1998.

41. Liu, Z., C. T. Chan and P. Sheng, "Three-component elastic wave band-gap material", *Physical Review B*, Vol. 65, No. 16, p. 165116, 2002.

42. Liu, Z., X. Zhang, Y. Mao, Y. Zhu, Z. Yang, C. Chan and P. Sheng, "Locally resonant sonic materials", *Science*, Vol. 289, No. 5485, pp. 1734–1736, 2000.

43. Hirsekorn, M., P. P. Delsanto, N. Batra and P. Matic, "Modelling and simulation of acoustic wave propagation in locally resonant sonic materials", *Ultrasonics*, Vol. 42, No. 1, pp. 231–235, 2004.

44. Goffaux, C. and J. Sánchez-Dehesa, "Two-dimensional phononic crystals studied using a variational method: Application to lattices of locally resonant materials", *Physical review B*, Vol. 67, No. 14, p. 144301, 2003.

45. Wang, G., X. Wen, J. Wen, L. Shao and Y. Liu, "Two-dimensional locally resonant phononic crystals with binary structures", *Physical review letters*, Vol. 93, No. 15, p. 154302, 2004.

46. Taniker, S. and C. Yilmaz, "Phononic gaps induced by inertial amplification in BCC and FCC lattices", *Physics Letters A*, Vol. 377, No. 31, pp. 1930–1936, 2013.

47. Taniker, S. and C. Yilmaz, "Generating ultra wide vibration stop bands by a novel inertial amplification mechanism topology with flexure hinges", *International Journal of Solids and Structures*, Vol. 106, pp. 129–138, 2017.

48. Acar, G. and C. Yilmaz, "Experimental and numerical evidence for the existence of

wide and deep phononic gaps induced by inertial amplification in two-dimensional solid structures", *Journal of Sound and Vibration*, Vol. 332, No. 24, pp. 6389–6404, 2013.

49. Yuksel, O. and C. Yilmaz, "Shape optimization of phononic band gap structures incorporating inertial amplification mechanisms", *Journal of Sound and Vibration*, Vol. 355, pp. 232–245, 2015.

50. Taniker, S. and C. Yilmaz, "Design, analysis and experimental investigation of three-dimensional structures with inertial amplification induced vibration stop bands", *International Journal of Solids and Structures*, Vol. 72, pp. 88–97, 2015.

51. Frandsen, N. M., O. R. Bilal, J. S. Jensen and M. I. Hussein, "Inertial amplification of continuous structures: Large band gaps from small masses", *Journal of Applied Physics*, Vol. 119, No. 12, p. 124902, 2016.

52. Li, J. and S. Li, "Generating ultra wide low-frequency gap for transverse wave isolation via inertial amplification effects", *Physics Letters A*, Vol. 382, No. 5, pp. 241–247, 2018.

53. Barys, M., J. S. Jensen and N. M. Frandsen, "Efficient attenuation of beam vibrations by inertial amplification", *European Journal of Mechanics-A/Solids*, Vol. 71, pp. 245 – 257, 2018.

54. Schmied, J. U., C. Sugino, A. Bergamini, P. Ermanni, M. Ruzzene and A. Erturk, "Toward structurally integrated locally resonant metamaterials for vibration attenuation", *Active and Passive Smart Structures and Integrated Systems 2017*, Vol. 10164, p. 1016413, International Society for Optics and Photonics, 2017.

55. Inman, D. J., *Engineering vibration*, Vol. 3, Prentice Hall New Jersey, 2008.

56. Delpero, T., G. Hannema, B. Van Damme, S. Schoenwald, A. Zemp and A. Bergamini, "Inertia amplification in phononic crystals for low frequency

bandgaps", *ECCOMAS Thematic Conference on Smart Structures and Materials*, pp. 1657–1668, CIMNE, 2017.

57. Zheng, B. and J. Xu, "Mechanical logic switches based on DNA-inspired acoustic metamaterials with ultrabroad low-frequency band gaps", *Journal of Physics D: Applied Physics*, Vol. 50, No. 46, p. 465601, 2017.

58. Love, A. E. H., *A treatise on the mathematical theory of elasticity*, Vol. 1, Cambridge University Press, 2013.

59. Wahl, A. M., *Mechanical springs*, Penton Publishing Company, 1944.

60. Witz, J. and Z. Tan, "On the axial-torsional structural behaviour of flexible pipes, umbilicals and marine cables", *Marine Structures*, Vol. 5, No. 2-3, pp. 205–227, 1992.

61. Phillips, J. W. and G. A. Costello, "Large deflections of impacted helical springs", *the Journal of the Acoustical Society of America*, Vol. 51, No. 3B, pp. 967–973, 1972.

62. Nagaya, K., "Stresses in a helical spring of arbitrary cross section with consideration of end effects", *Journal of vibration, acoustics, stress, and reliability in design*, Vol. 109, No. 3, pp. 289–301, 1987.

63. Przemieniecki, J. S., *Theory of matrix structural analysis*, Courier Corporation, 1985.

64. Yokoyama, T., "Vibrations of a hanging Timoshenko beam under gravity", *Journal of Sound and Vibration*, Vol. 141, No. 2, pp. 245–258, 1990.

65. Cowper, G., "The shear coefficient in Timoshenko's beam theory", *Journal of applied mechanics*, Vol. 33, No. 2, pp. 335–340, 1966.

66. Kim, H.-W., J.-S. Jang, W.-S. Yoo, O. Dmitrochenko and A. Mikkola, "Helix beam

model of a coil spring including twisting effect to capture lateral deformation", *International Journal of Precision Engineering and Manufacturing*, Vol. 14, No. 9, pp. 1615–1622, 2013.

67. Wang, R., X. Zhou, Z. Zhu and Q. Liu, "Compliant linear-rotation motion transduction element based on novel spatial helical flexure hinge", *Mechanism and Machine Theory*, Vol. 92, pp. 330–337, 2015.

68. Lobontiu, N., *Compliant mechanisms: design of flexure hinges*, CRC press, 2002.

69. Trease, B. P., Y.-M. Moon and S. Kota, "Design of large-displacement compliant joints", *Journal of mechanical design*, Vol. 127, No. 4, pp. 788–798, 2005.

70. Wu, J., S. Cai, J. Cui and J. Tan, "A generalized analytical compliance model for cartwheel flexure hinges", *Review of Scientific Instruments*, Vol. 86, No. 10, p. 105003, 2015.

71. Chen, N., X. Chen, Y. Wu, C. Yang and L. Xu, "Spiral profile design and parameter analysis of flexure spring", *Cryogenics*, Vol. 46, No. 6, pp. 409–419, 2006.

72. Ozkaya, E. and C. Yilmaz, "Effect of eddy current damping on phononic band gaps generated by locally resonant periodic structures", *Journal of Sound and Vibration*, Vol. 389, pp. 250–265, 2017.

73. Zhou, W., L. Wang, Z. Gan, R. Wang, L. Qiu and J. Pfotenhauer, "The performance comparison of Oxford and Triangle flexure bearings", *AIP Conference Proceedings*, Vol. 1434, pp. 1149–1156, AIP, 2012.

74. Khot, M. and B. Gawali, "Finite element analysis and optimization of flexure bearing for linear motor compressor", *Physics Procedia*, Vol. 67, pp. 379–385, 2015.

75. VR, R. and B. T. Kuzhiveli, "Modelling and failure analysis of flexure springs for a Stirling cryocooler", *Journal of Engineering Science and Technology*, Vol. 12,

No. 4, pp. 888–897, 2017.

76. Mennitto, G. and M. Buehler, "Experimental validation of compliance models for LADD transmission kinematics", *Intelligent Robots and Systems 95.'Human Robot Interaction and Cooperative Robots', Proceedings. 1995 IEEE/RSJ International Conference on*, Vol. 1, pp. 385–390, IEEE, 1995.

APPENDIX A: MATRIX CONSTANTS

Element stiffness matrix constants

A=Cross-section area

E=Young's modulus

L=Element length

G=Shear modulus

J=Torsional moment of inertia

J_x=Polar moment of inertia in x direction $(I_y + I_z)$

A^s=Shear area normal to direction

$a_z = a(I_z, \phi_y)$

$a_y = a(I_y, \phi_z)$

$c_z = a(I_z, \phi_y)$

$c_y = a(I_y, \phi_z)$

$e_z = a(I_z, \phi_y)$

$e_y = a(I_y, \phi_z)$

$f_z = a(I_z, \phi_y)$

$f_y = a(I_y, \phi_z)$

$$\phi_y = \frac{12EI_z}{GA_z^s L^2} \tag{A.1}$$

$$\phi_z = \frac{12EI_y}{GA_y^s L^2} \tag{A.2}$$

$$a(I, \phi) = \frac{12EI}{L^3(1+\phi)} \tag{A.3}$$

$$c(I,\phi) = \frac{6EI}{L^2(1+\phi)} \tag{A.4}$$

$$e(I,\phi) = \frac{(4+\phi)EI}{L(1+\phi)} \tag{A.5}$$

$$f(I,\phi) = \frac{(2-\phi)EI}{L(1+\phi)} \tag{A.6}$$

Sum of local and gravity stiffness matrix($[K_l]$+$[K_g]$) constants ϕ_z is used in capital A constants and ϕ_y is used in capital B constants. To prevent repeated equations only A constants is written. In addition, beam is divided into m equal parts. The change of the stiffness due to gravity within the $(n+1)^{th}$ beam element given in the expressions below.

$$A_{11} = (\frac{6}{5} + 2\phi_z + \phi_z^2)\frac{(m-n)}{(1+\phi_z)^2} + (\frac{3}{5} + \phi_z + \frac{\phi_z^2}{2})\frac{1}{(1+\phi_z)^2} \tag{A.7}$$

$$A_{12} = \frac{L}{10}\frac{(m-n)}{(1+\phi_z)^2} + (\frac{1}{10} + \frac{2\phi_z}{15} + \frac{\phi_z^2}{12})\frac{L}{(1+\phi_z)^2} \tag{A.8}$$

$$A_{13} = -(\frac{6}{5} + 2\phi_z + \phi_z^2)\frac{(m-n)}{(1+\phi_z)^2} - (\frac{3}{5} + \phi_z + \frac{\phi_z^2}{2})\frac{1}{(1+\phi_z)^2} \tag{A.9}$$

$$A_{14} = \frac{L}{10}\frac{(m-n)}{(1+\phi_z)^2} - (\frac{2\phi_z}{15} + \frac{\phi_z^2}{12})\frac{L}{(1+\phi_z)^2} \tag{A.10}$$

$$A_{22} = (\frac{2}{15} + \frac{\phi_z}{6} + \frac{\phi_z^2}{12})\frac{(m-n)L^2}{(1+\phi_z)^2} + (\frac{1}{30} + \frac{\phi_z}{20} + \frac{\phi_z^2}{24})\frac{L^2}{(1+\phi_z)^2} \tag{A.11}$$

$$A_{23} = \frac{L}{10}\frac{(m-n)}{(1+\phi_z)^2} - (\frac{1}{10} + \frac{2\phi_z}{15} + \frac{\phi_z^2}{12})\frac{L}{(1+\phi_z)^2} \tag{A.12}$$

$$A_{24} = -(\frac{1}{30} + \frac{\phi_z}{6} + \frac{\phi_z^2}{12})\frac{(m-n)L^2}{(1+\phi_z)^2} - (\frac{1}{60} + \frac{\phi_z}{12} + \frac{\phi_z^2}{24})\frac{L^2}{(1+\phi_z)^2} \tag{A.13}$$

$$A_{33} = (\frac{6}{5} + 2\phi_z + \phi_z^2)\frac{(m-n)}{(1+\phi_z)^2} + (\frac{3}{5} + \phi_z + \frac{\phi_z^2}{2})\frac{1}{(1+\phi_z)^2} \tag{A.14}$$

$$A_{34} = -\frac{L}{10}\frac{(m-n)}{(1+\phi_z)^2} + (\frac{2\phi_z}{15} + \frac{\phi_z^2}{12})\frac{L}{(1+\phi_z)^2} \tag{A.15}$$

$$A_{44} = (\frac{2}{15} + \frac{\phi_z}{6} + \frac{\phi_z^2}{12})\frac{(m-n)L^2}{(1+\phi_z)^2} + (\frac{1}{10} + \frac{7\phi_z}{60} + \frac{\phi_z^2}{24})\frac{L^2}{(1+\phi_z)^2} \tag{A.16}$$

Dr. Yokoyoma element mass matrix($[M_l]$) constants

ρ=Density

m=Added mass per unit length

ϵ=Prestrain

M_t=$(\rho A + m)L(1-\epsilon)$

r_y, r_z=Radius of gyrations

$A_z = a(r_z, \phi_y)$

$A_y = a(r_y, \phi_z)$

$B_z = a(r_z, \phi_y)$

$B_y = a(r_y, \phi_z)$

$C_z = a(r_z, \phi_y)$

$C_y = a(r_y, \phi_z)$

$D_z = a(r_z, \phi_y)$

$D_y = a(r_y, \phi_z)$

$E_z = a(r_z, \phi_y)$

$E_y = a(r_y, \phi_z)$

$F_z = a(r_z, \phi_y)$

$F_y = a(r_y, \phi_z)$

$$r_y = \sqrt{\frac{I_y}{A}} \tag{A.17}$$

$$r_z = \sqrt{\frac{I_z}{A}} \tag{A.18}$$

$$A(r,\phi) = \frac{(\frac{13}{35} + \frac{7\phi}{10} + \frac{\phi^2}{3} + \frac{6r^2}{5L^2})}{(1+\phi)^2} \tag{A.19}$$

$$B(r,\phi) = \frac{(\frac{9}{70} + \frac{3\phi}{10} + \frac{\phi^2}{6} - \frac{6r^2}{5L^2})}{(1+\phi)^2} \tag{A.20}$$

$$C(r,\phi) = \frac{(\frac{11}{210} + \frac{11\phi}{120} + \frac{\phi^2}{24} + (\frac{1}{10} - \frac{\phi}{2})(\frac{r}{L})^2)L}{(1+\phi)^2} \tag{A.21}$$

$$D(r,\phi) = \frac{(\frac{13}{420} + \frac{3\phi}{40} + \frac{\phi^2}{24} - (\frac{1}{10} - \frac{\phi}{2})(\frac{r}{L})^2)L}{(1+\phi)^2} \tag{A.22}$$

$$E(r,\phi) = \frac{(\frac{1}{105} + \frac{\phi}{60} + \frac{\phi^2}{120} + (\frac{2}{15} + \frac{\phi}{6} + \frac{\phi^2}{3})(\frac{r}{L})^2)L^2}{(1+\phi)^2} \tag{A.23}$$

$$F(r,\phi) = \frac{(\frac{1}{140} + \frac{\phi}{60} + \frac{\phi^2}{120} + (\frac{1}{30} + \frac{\phi}{6} - \frac{\phi^2}{6})(\frac{r}{L})^2)L^2}{(1+\phi)^2} \tag{A.24}$$